Fan Noise Predictions of the NASA Source Diagnostic Test using Unsteady Simulations with LAVA Part I: Near-Field Aerodynamics and Turbulence

Luis S. Fernandes[*], Jeffrey A. Housman[†]
Gaetan K. Kenway[‡], Gerrit-Daniel Stich[§] and Cetin C. Kiris[¶]
NASA Ames Research Center, M/S 258-2, Moffett Field, California, 94035

A sliding mesh technique within the Launch, Ascent, and Vehicle Aerodynamics (LAVA) computational framework is validated using the experimental dataset collected as part of the NASA Source Diagnostic Test (SDT) campaign. Two modeling approaches are explored: the unsteady Reynolds-Averaged Navier Stokes (URANS) with Spalart-Allmaras (SA) turbulence model closure, and a hybrid Reynolds-Averaged Navier Stokes/Large Eddy Simulation (RANS/LES) paradigm employing a Zonal Detached Eddy Simulation (ZDES) closure with enhanced shielding protection. Fan stage performance metrics, aerodynamic quantities and turbulent flow structures are analyzed in this work. Initial studies focusing on grid and time-step sensitivity are presented. Sensitivity to different variants of the SA turbulence model is analyzed, supporting the use of the baseline SA model in the production runs. Two conditions are analyzed in detail using URANS and hybrid RANS/LES (HRLES). Mean flow quantities are well-captured by both methods in the low-speed (approach) regime. While URANS misses all the upstream-propagating noise in the inlet due to the rotor-locked tones being evanescent in nature at subsonic fan tip speeds, HRLES captures this broadband component in its pressure field. At the high-speed (sideline) condition, URANS shows better agreement with the SDT data than HRLES in the interstage flow-field. In this regime, URANS captures the tonal content propagating through the inlet, since the tones are now cut-on. Both methods are suitable to capture fan stage performance metrics and mean flow quantities, but only HRLES is able to resolve the fine turbulent structures responsible for broadband noise. The results support the use of the sliding mesh technique implemented in this work for future turbomachinery applications within the LAVA solver framework.

I. Nomenclature

C_p	=	Pressure coefficient	AST	=	Advanced Subsonic Technology
$C_{f,x}$	=	Axial skin friction coefficient	BPF	=	Blade-Passing Frequency
D_f	=	Fan diameter	HRLES	=	Hybrid RANS/LES
M_∞	=	Wind tunnel Mach number	LDV	=	Laser Doppler Velocimetry
R_f	=	Refinement factor	LES	=	Large Eddy Simulation
T_{rev}^n	=	Number of timesteps per revolution	LSWT	=	Low Speed Anechoic Wind Tunnel
U, V_θ, V_r	=	Mean velocity components	OGV	=	Outlet Guide Vane
u, v_θ, v_r	=	Velocity fluctuations	RANS	=	Reynolds-Averaged Navier Stokes
$\|\mathbf{\Omega}\|$	=	Vorticity magnitude	URANS	=	Unsteady Reynolds-Averaged Navier Stokes

[*]Research Scientist, Science and Technology Corporation, Computational Aerosciences Branch, AIAA Member, luismsfern@nasa.gov

[†]Research Scientist, Computational Aerosciences Branch, AIAA Senior Member, jeffrey.a.housman@nasa.gov

[‡]Research Scientist, Science and Technology Corporation, Computational Aerosciences Branch, AIAA Member, gaetan.k.kenway@nasa.gov

[§]Research Scientist, Science and Technology Corporation, Computational Aerosciences Branch, AIAA Member, gerrit-daniel.stich@nasa.gov

[¶]Computational Aerosciences Branch Chief, AIAA Senior Member, cetin.c.kiris@nasa.gov

II. Introduction

As a means to improve commercial aviation turbofan engine efficiency, the development trend continues to favor an increase in the bypass ratio, resulting in lower fan rotational speeds and jet exhaust velocities. This is usually accompanied by an increase in the fan diameter and a shortening of the nacelle to reduce weight and viscous drag. Ultra-high bypass ratio turbofan engines are a near-term solution promising higher efficiency and a reduction in noise levels to tackle the ever-increasing demands of urban air traffic, as the efficiency limits of conventional turbofan engines near the horizon. This trend has led to higher fan-to-jet noise ratios, and resulted in fan noise dominating the engine total flyover noise footprint at both takeoff and approach conditions [1]. This motivates work towards improving the capabilities of modern computational fluid dynamics (CFD) tools for accurate fan noise predictions, setting a path forward towards Certification and Qualification by Analysis, allowing less expensive testing and development of fan noise reduction technologies.

An important component of developing this toolset is validation. NASA conducted an extensive aircraft noise reduction effort through the Advanced Subsonic Technology (AST) program in the mid-1990s [1]. Several experimental tests were performed as part of the AST program, many of which had the goal of identifying and characterizing the main noise generation mechanisms within a turbofan engine. An experimental campaign that resulted from this program was the NASA Source Diagnostic Test (SDT), conducted at the NASA John H. Glenn Research Center 9×15 ft. Low Speed Anechoic Wind Tunnel (LSWT). Pictures collected during this campaign are shown in Fig. 1. Extensive analysis and discussion of the results gathered in the test are available in Podboy et al. [2], Hughes et al. [3], Hughes [4], Heidelberg [5], Premo and Joppa [6], Woodward et al. [7], Envia [8], Podboy et al. [9]. This comprehensive dataset will be used in the present work as a validation test case for the Launch, Ascent, and Vehicle Aerodynamics (LAVA) solver framework [10] in the context of fan noise generation and far-field propagation, particularly when it comes to the accuracy provided by explicitly simulating the rotating geometric components using a recently-implemented sliding mesh technique.

(a) Rotor-alone configuration - frontal view.   (b) Rotor-alone configuration - side view.   (c) Full configuration - frontal view.
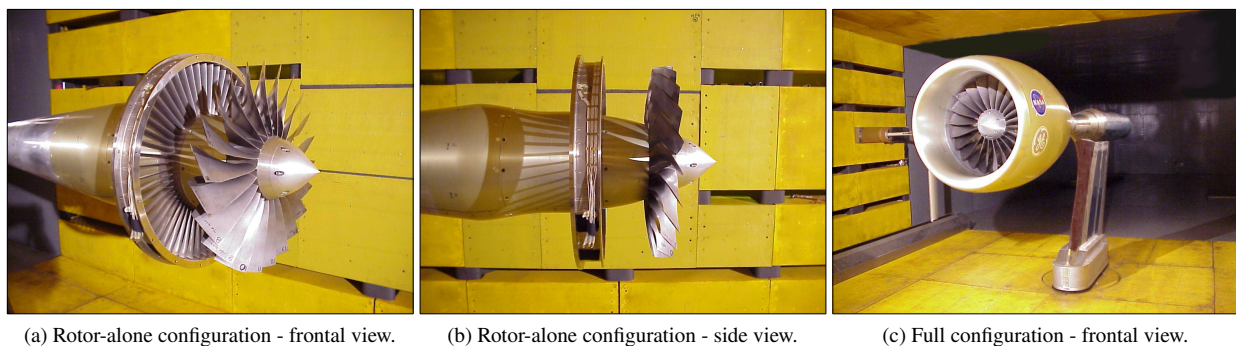
Fig. 1   Source Diagnostic Test (SDT) fan model installed in the NASA John H. Glenn Research Center 9×15 ft. Low Speed Anechoic Wind Tunnel (LSWT) [4]. Rotor-alone (RAN) configuration (left and center) - not considered in this work - and full configuration with nacelle (right) studied in the present work.

The complex fan rig configuration in the NASA SDT has been the subject of many computational studies in the recent past, brought forth by an interest in characterizing the broadband noise-generating flow inside the fan stage, and evaluate the assumptions utilized by analytical models that avoid the complexity of turbomachinery configurations. Hah et al. [11] studied the development of the fan blade wakes on a modified configuration composed of 22 fan and 22 outlet-guide-vane (OGV) blades using both unsteady Reynolds-Averaged Navier-Stokes Simulation (URANS) and Large Eddy Simulation (LES) methods. Moreau [12] compiled a series of results comparing URANS and LES acoustic computations to analytical methods. While reliable tonal noise predictions can be obtained with URANS, broadband noise requires resolving of the small turbulent scales with methods such as LES or Lattice-Boltzmann (LBM). The latter has been applied to the SDT using the PowerFLOW solver for fan operating conditions representative of approach [13] and take-off [14]. Overall Sound Pressure Levels (OASPL) along a sideline microphone array showed good agreement with the SDT data, and evidence of buzz-saw noise originating from Multiple Pure Tones (MPT) was presented when the fan blade placements were not exactly periodically spaced. Small deviations in the range of ±0.25° were sufficient to redistribute up to 6 dB of the tonal acoustic energy originally present in the first two blade-passing frequencies (BPF). Shur et al. [15–17] also presented a thorough investigation of the aerodynamic and aeroacoustic differences of simulating the SDT fan rig with URANS and hybrid RANS/LES. Their findings solidify the necessity of resolving the

small-scale turbulence to accurately predict the broadband noise levels.

Two modeling paradigms are considered in the present work: URANS with the Spalart-Allmaras (SA) turbulence model closure (and its variants) and a hybrid RANS/LES approach with a Zonal Detached Eddy Simulation (ZDES) closure employing an enhanced protection of attached boundary layers [18]. Both approaches are evaluated in their ability to capture the interstage flow physics and the turbulent content contained therein. Special attention was given to the grid in this region to properly resolve the fan blades and wakes, as these will ultimately dictate the amplitude of the fan/stator interaction noise at harmonics of the BPF. The work will be split into two parts. This paper will focus on the aerodynamic and turbulent characteristics of the flow-field and its validation against the SDT data, while a second paper will be published at a later date focusing on the acoustics of this test case using the two computational methods considered.

The paper is organized as follows. An introduction of the test case will be given in Sec. II.A, followed by a summary of the relevant experimental data gathered in the SDT in Sec. II.B. The computational methodology is portrayed at length in Sections III.A through III.E, starting with the turbulent closures considered and the numerical discretizations utilized, and ending with a description of the sliding mesh implementation used to model the rotating fan inside the stage. A thorough discussion of several sensitivity studies is then provided in Sec. IV.A, followed by a comparison of results from both URANS and hybrid RANS/LES for both the low-speed (Sec. IV.B) and high-speed (Sec. IV.C) flow regimes. A summary of the computational cost for the production runs analyzed in this work is given in Sec. V. Conclusions are formulated in Sec. VI.

A. Problem Description

The test rig considered in the present work employs the primary test rotor, designated R4, with a diameter D_f of 0.5572 m, and composed of 22 identical blades. Three distinct OGV designs were considered in the experiment, from which the baseline OGV, consisting of 54 unswept equally-spaced blades, will be analyzed in this work. A spinner connects to the centerbody strut support arm, which was attached to the wind tunnel floor in the experimental setup. Five fan rotational speeds were considered in the experiment, ranging from an approach (low-speed) operating condition of 7808 rotations per minute (RPM) (or 61.7 % of the design speed) to a sideline/take-off (high-speed) condition of 12,657 RPM (or 100 % of the design speed). Both low-speed and high-speed conditions (7808 RPM and 12,657 RPM, respectively) will be analyzed in this work. These operating conditions represent vastly different flow-field regimes in an attempt to explore the current capabilities of the LAVA solver framework for turbomachinery applications. The rotor tip Mach number for these conditions spans between 0.6694 and 1.085 based on the freestream speed of sound.

The wind tunnel freestream Mach number is M_∞ = 0.1, representative of takeoff and landing conditions. An extensive dataset was collected during the experiment for validation of different numerical approaches. Single-point hot-wire probe measurements at two different axial stations in the interstage region allow characterization of the rotor wake [2]. Laser Doppler velocimetry (LDV) measurements at different survey locations are also available [2, 9] for quantification of the wake flow, blade tip flow and shock location in the fan stage (high-speed case only). Overall fan stage performance results are compiled in [3, 4] for both a rotor-alone nacelle system and the complete engine configuration with the OGVs. Regarding acoustics, the dataset contains tonal mode measurements [5], a spinning mode decomposition of the wall sound pressure levels (SPL) [6], and far-field SPL measured along a sideline translating microphone probe. A brief description of the data processing performed and the location of the measuring probes is provided below.

B. Experimental Data Assessment

1. Velocity Data

Single-point hot-wire probe measurements at station x = 0.1016 m were collected to quantify the velocity field downstream of the fan wake. Figure 2a illustrates where the data collection takes place with respect to the fan stage. The dataset contains axial, tangential and radial velocity measurements acquired at a sampling rate of 200 kHz for a duration of 1 second, totaling 129 fan revolutions. If each revolution represents an ensemble, and because all fan blades are identical and equally spaced circumferentially, each blade passage may be taken as a sub-ensemble. The raw data is averaged over the 129 ensembles to obtain the ensemble-averaged mean flow components. These are then averaged once more over the 22 sub-ensembles to obtain the final mean flow footprint across each blade pass. The resulting mean flow is then subtracted from the raw data to obtain the instantaneous fluctuation velocity field. A similar averaging procedure then takes place acting on these fluctuating components, this time using root-mean-square (RMS) rather than arithmetic

averaging.

The time series data collected over the course of 1 second allows an analysis of the frequency content of the velocity field. A subset of 6 hot-wire probe locations were chosen from the total of 50 to quantify the frequency content in regions located at different radii along station 1. These are visually depicted in Fig. 2b. Fourier transforms are computed with a bandwidth of 58.5 Hz from both the hot-wire data and the data sampled from the numerical simulations, and smoothed using Hann weighting with a 50 % window overlap to reduce spectral leakage.

(a) Location of hot-wire probe station 1 in the interstage region.

(b) Subset of locations from hot-wire probe used in velocity spectra comparisons.
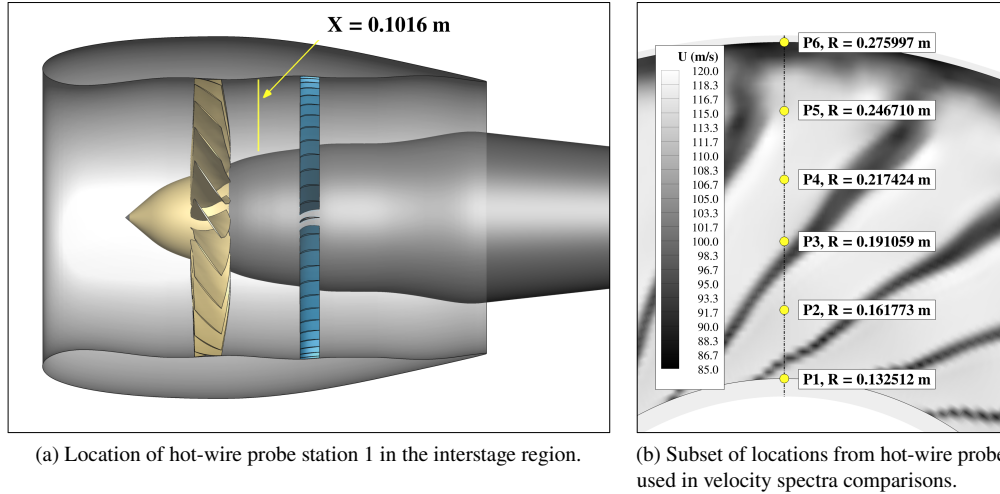
Fig. 2   Velocity measurement probes location in the NASA SDT.

2. Microphone Data

Acoustic data extraction took place in the NASA SDT experiment along a sideline 2.26822 m away from the fan stage centerline. The geometric polar angles ranging from 27.2° to 130° are covered with 5° resolution along this traversing sideline, while 3 additional microphones were fixed further downstream, covering the polar angles of 136°, 147° and 158°, for a total of 47 microphone locations. These locations are illustrated in Fig. 3.
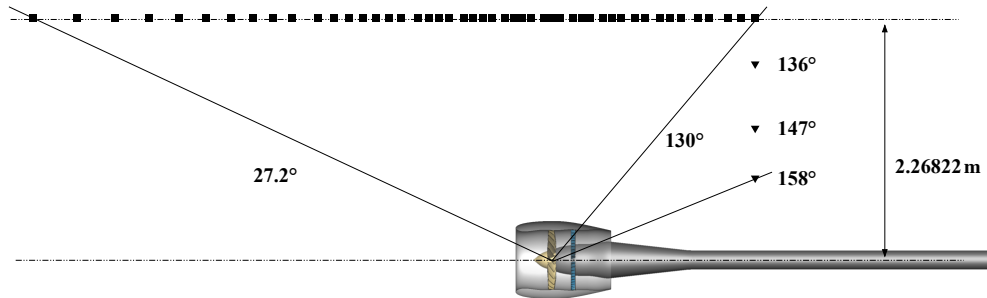

Fig. 3   Acoustic measurement probes location in the NASA SDT. Sideline microphone (■) and fixed microphone (▾) arrays shown.

III. Computational Methodology

The CFD solver used in the present work is part of the Launch, Ascent, and Vehicle Aerodynamics (LAVA) solver framework [10]. This flexible computational framework was developed with highly complex geometries in mind. As such, it supports a variety of mesh paradigms, such as the structured Cartesian, curvilinear overset and unstructured arbitrary polyhedral. In the present work, the curvilinear overset mesh paradigm is employed. Both Message Passing

Interface (MPI) and OpenMP protocols are leveraged to achieve a highly scalable, parallel, HPC (High Performance Computing) code.

A. Turbulence Model Closures

Two modeling approaches are considered in the present work to simulate the SDT fan stage configuration: the Unsteady Reynolds-Averaged Navier Stokes (URANS), and the scale-resolving hybrid RANS/LES (HRLES). For the URANS studies discussed in the present work, the Favre-averaged RANS system of equations is closed using the Spalart-Allmaras (SA) turbulence model [19] and variants thereof. Four corrections to the baseline model have been investigated, namely: SA with the Rotation/Curvature correction (SA-RC)[†] [20]; SA with the Quadratic Constitutive Relation, version 2000 (SA-QCR) [21]; SA with both RC and QCR corrections applied (SA-RC-QCR); SA with the mixing layer compressibility correction (SA-CC) [22]. This modeling paradigm lacks the ability to capture the level of fine-grained turbulent content required to accurately predict broadband noise, and is thus only expected to capture tonal noise at BPF harmonics.

On the other hand, HRLES employs a scale-resolving Zonal Detached Eddy Simulation (ZDES) model that provides Large Eddy Simulation (LES) behavior everywhere in the flow-field (LES mode) except for thin near-wall regions in attached boundary layers, where a RANS closure is applied (RANS mode). These flow regions are detected by the model using a shielding function f_d which protects the attached boundary layers from LES mode treatment ($f_d = 1$). This added complexity is justified since RANS models accurately predict boundary layer development at a fraction of the computational cost that LES would require. The specific model used in this work is the ZDES 2020 Mode 2 Enhanced Protection (ZDES2020-Mode2-EP) [18]. There are two main developments in the ZDES2020-Mode2-EP model over previous iterations of HRLES closures such as Detached Delayed Eddy Simulation 2006 (DDES2006) [23] and ZDES2012-Mode2 [24]. Firstly, it employs an improved shielding function offering better protection for zones that should stay in RANS mode ($f_d = 0$), preventing the well-known model stress depletion behavior [25] in under-resolved regions of the flow. The model also minimizes the delay observed in LES content creation when transitioning from RANS to LES mode in hybrid RANS/LES of free shear layer flows. The ZDES2020-Mode2-EP model has been previously validated and used in LAVA [26–29], and the reader is encouraged to review these for implementation-specific details. Finally, the turbulence model closure applied in the HRLES simulations for zones in RANS mode is the baseline SA model.

B. Numerical Discretization

A conservative finite-difference formulation is applied to the flow equations for non-orthogonal curvilinear coordinates in strong conservation law form [30]. An implicit second-order backwards differencing formula is used for time integration, and the discretized equations are marched in pseudo-time until a sufficient reduction in the residuals has been achieved for each physical time-step. Sub-iteration nonlinear convergence is accelerated by ramping up the Courant-Friedrichs-Lewy (CFL) number during the initial solution transient. In the present computations, approximately 4 to 5 orders of magnitude reduction in the flow-field and turbulence variable residual is achieved when using URANS, while HRLES typically achieves 3 to 4 orders of magnitude reduction in the flow-field variable residual and 2 to 3 orders in the turbulence variable residual. A Geometric Conservation Law (GCL) preserving time-varying metric term discretization is used for the moving grid system [31]. Additionally, a second-order convective flux discretization, consisting of a modified Roe scheme with blended third-order upwind-biased and fourth-order centered reconstruction operators for left and right state reconstruction to the mid-points [32], is used in the present work. A blending factor ζ of 1 % is applied to the upwind-biased contribution whenever blending is active, effectively lowering the amount of numerical dissipation in turbulence-producing regions of the flow. For URANS simulations, a 1 % upwind fixed blending reconstruction was employed, whereas for HRLES the shielding function f_d is used to determine whether blending is performed ($f_d > 0.8$) or not (pure upwind-biased reconstruction).

C. Geometry and Computational Domain

The baseline SDT configuration, shown in Fig. 2a, is composed of four main components: nacelle, centerbody, the R4 fan and the baseline OGV blade row. The origin of the coordinate system is located at the axial location corresponding to the midpoint of the rotor along the centerline. The nacelle length is about 1.6 D_f, extending from

---

[†]The current implementation of the Rotation/Curvature correction in the LAVA solver framework neglects the time-derivative of the strain-rate tensor $\partial S_{ij}/\partial t$ from the Reynolds transport terms $\mathrm{D}S_{ij}/\mathrm{D}t$.

$x = -0.3305$ m to $x = 0.5587$ m. The 0.5 mm gap between the rotor blade tip and the shroud is resolved in all simulations considered. The spinner part of the centerbody entends from the nose until an axial coordinate of $x = 0.0424$ m (surface shaded in yellow in Fig. 2a). Downstream of this junction, the centerbody is stationary, and the wall boundary conditions applied in the computational setup properly reflect this behavior. Finally, the nacelle exit diameter is $D_e = 0.542$ m.

The wind tunnel mounting hardware was not modeled in the present work, so as to avoid the additional complexity and potential noise sources due to interactions of the shear layer flow-field with these components. Correspondingly, the centerbody is extended axially all the way to the far-field downstream end of the computational domain as a means to smoothly transition from the resolved near-field region to the under-resolved far-field. The incoming flow is aligned with the fan axis with a Mach number of 0.1. Farfield Riemann invariant boundary conditions are applied at the boundaries of the computational domain, with ambient static conditions of $P_{ref} = 101,325$ Pa and $T_{ref} = 288.15$ K. Adiabatic viscous wall boundary conditions are applied at every wall in the domain. The computational domain is discretized using a set of structured curvilinear meshes, coupled using an overset grid paradigm [33] and a new sliding mesh interface methodology added to couple static and rotating mesh regions. More details on the implementation of the methodology are provided in Sec. III.E.

D. Overset Grid Topologies

An overview of the near-body structured curvilinear grid topologies around the fan stage is shown in Fig. 4a, which contains slices of relevant grid blocks prior to the optimized hole-cutting procedure [34] taking place for clarity purposes. Most internal flow grids consist of block-structured point-matched grids, with the exception of the ones resolving the rotor and OGV blade geometries. These use overset to communicate with the nacelle inflow, interstage and outflow grid blocks. The grid sections shown are revolved 360° around the fan axis with varying circumferential grid point counts, with the exception of the off-body grid block covering the spinner nose tip to remove the singularity that would otherwise occur. This block overlaps with the volume grid grown from a small surface cap grid covering the very tip of the spinner nose. Cartesian grid blocks with a 2:1 coarsening ratio create a smooth transition between the near-field and the far-field. Body-fitted topologies of the fan and OGV blade grids are illustrated in Figs. 4b and 4c. An O-grid topology was selected to resolve the boundary layers that form as the blades cut through the incoming flow. The wakes that develop downstream of each blade are captured through localized refinement, either via an additional block that follows the complex shape of the fan blade wakes (as shown in Fig. 4b) or via adequate grid point clustering of the blocks surrounding the OGV stage (as Fig. 4c illustrates).

The grid spacings used in the near-body grids are dictated by acoustic wave propagation requirements for the noise assessment part of this study (to be published in a future date). To understand these spacing requirements for the numerical discretization employed in the fan stage simulations, a simplified 1D problem was set up. A time-dependent point source emitting pressure waves at frequencies matching BPF_1 and BPF_2 (2862.93 Hz and 5725.87 Hz, respectively) was placed in a Mach 0.1 freestream to model the tonal noise signature of the fan stage. Two receiver probes (one upstream and one downstream) were then used to capture the propagated acoustic signal at distances associated with those between the R4 rotor blades and the Ffowcs Williams and Hawkings (FW-H) surfaces in the fan stage. A family of grids with an increasing number of points-per-wavelength (PPW) was then generated, ranging between 5 PPW and 50 PPW. This 1D study showed that at least 15 PPW are required to capture tones of BPF_2 with amplitudes within 3 dB of the finest (50 PPW) mesh calculations, corresponding to a grid spacing of 4.25 mm. The final grid system satisfies this constraint in all three directions everywhere inside the FW-H surface used to capture the near-field acoustic signal. Additional metrics for each grid used in the present work are provided in Sec. IV.A.1.

E. Sliding Mesh Implementation

A sliding mesh technique was implemented in the LAVA solver framework to allow the simulation of components in relative rotating motion. Solution information is exchanged between each pair of grid zones in relative motion across a sliding mesh interface. In the current implementation, this interface must obey the following rules:

1) It must be shared by both grid zones in relative motion, i.e., the two grids must be block-to-block point-matching at the interface in the initial grid configuration;
2) Interface nodes must be exactly circumferential, resulting in a set of ring-like strips of cells at different radii;
3) It must have equally spaced nodes in the circumferential direction.

An example of a valid interface is depicted in Fig. 5a. This implementation of a sliding mesh capability poses a restriction early in the process of mesh generation, but guarantees that each donor node will always remain in the same cell ring as the two grids rotate over time. This feature removes the costly donor cell spatial search from the process,
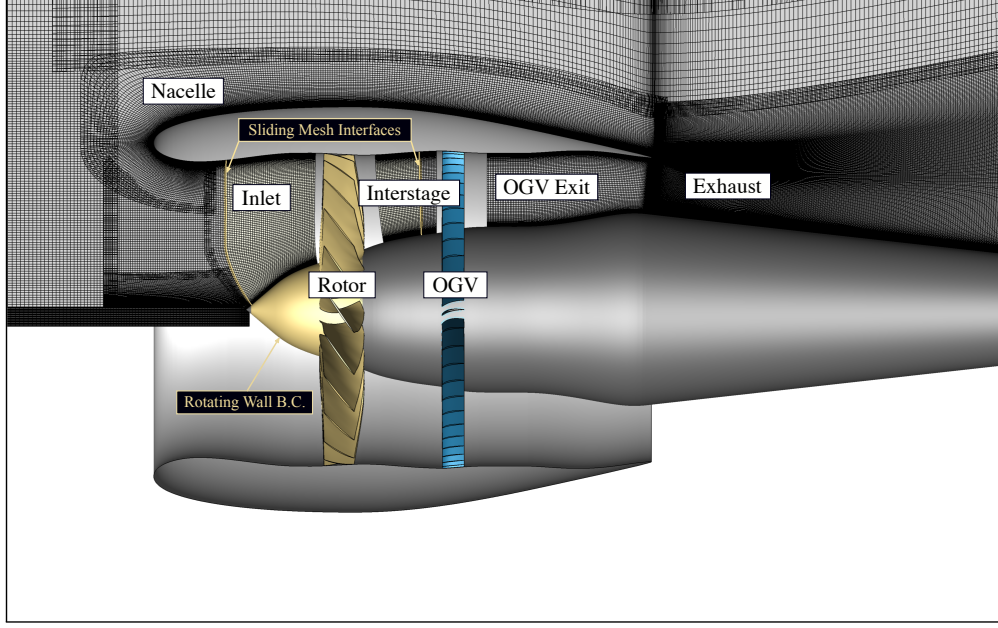
(a) Overview of fan stage near-body grid topologies.
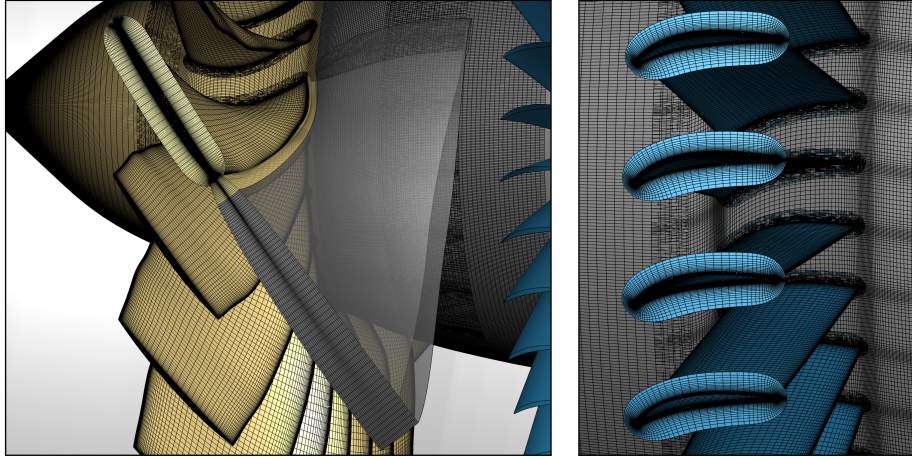
(b) O-grid topology used for fan blade with wake-resolving grid.

(c) O-grid topology used for OGV blades.

Fig. 4   Overview of grid topologies employed in the hybrid RANS/LES simulations.

which would otherwise need to be performed at each time-step. Instead, once the circumferential coordinate of the node currently looking for its donor information $\theta_{j,k}$ is computed, the two donor nodes are immediately defined as the two neighboring nodes whose θ^d interval encompasses $\theta_{j,k}$. Once the donor information is known, a simple 1D interpolation in θ-space is performed to obtain the ghost node values at the interface:

$$\phi_{j,k} = \phi_{j,k}^d + \left(\theta_{j,k} - \theta_{j,k}^d\right)\left(\frac{\phi_{j+1,k}^d - \phi_{j,k}^d}{\theta_{j+1,k}^d - \theta_{j,k}^d}\right), \tag{1}$$

where ϕ is any of the five primitive variables (p, u, v, w, T) or turbulence variable $\tilde{\nu}$, and d stands for donor. This procedure is illustrated in Fig. 6. The implementation of this model in the LAVA solver has been verified and validated against published data [35, 36], and will be evaluated in the present work using the SDT experimental data as reference.
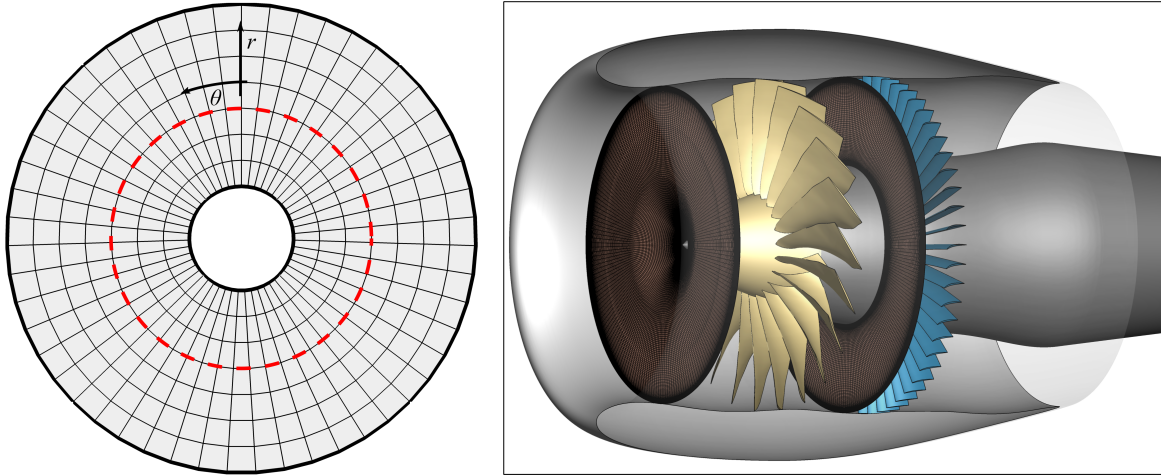
(a) Example of a valid topology for a constant-radius sliding mesh interface.

(b) Sliding mesh interface employed in the SDT case. Every 4th grid line is shown in the circumferential direction for visualization purposes.

Fig. 5   Overview of grid topologies employed in the hybrid RANS/LES simulations.
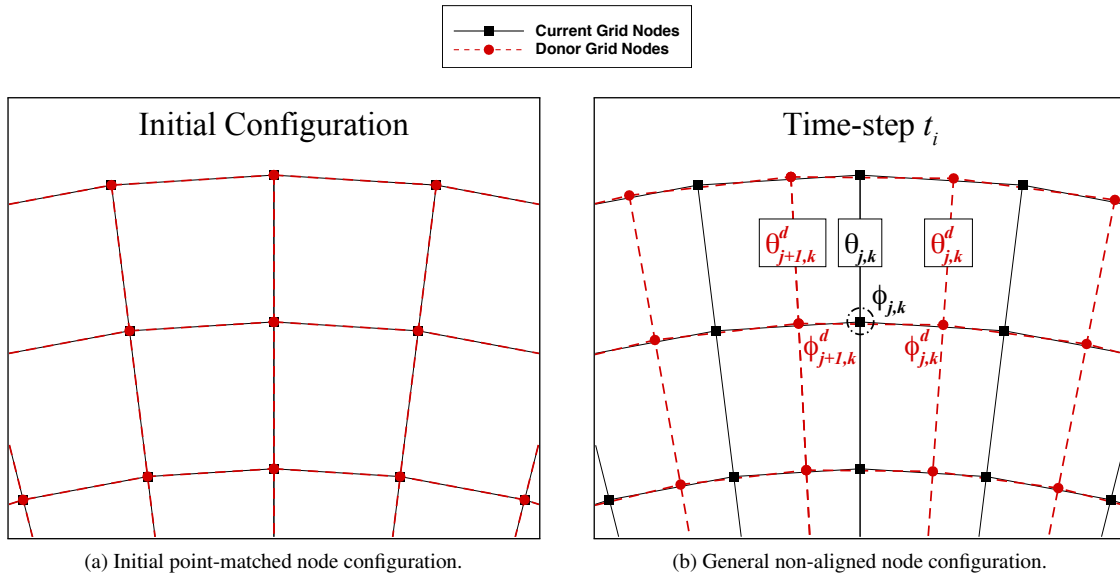
(a) Initial point-matched node configuration.

(b) General non-aligned node configuration.

Fig. 6   Node locations at a sliding mesh interface in the initial configuration and at any given time-step.

IV. Results and Discussion

Several studies were performed to gain insight on the degree of solution sensitivity to different parameters. These are presented in Sec. IV.A, followed by a thorough comparison of numerical and experimental data for both low-speed (Sec. IV.B) and high-speed (Sec. IV.C) regimes.

The procedure used to generate the reported results will now be described in detail. Unless otherwise noted, the initialization procedure for each case proceeded as follows:

1) Initialize the flow-field with freestream conditions and allow the fan's rotational speed to establish the initial low-order flow features, using a coarse time-step corresponding to 176 time-steps per fan revolution and a CFL of 10;

2) Ramp up the CFL to 100 and allow for 10 fan revolutions to further develop the flow without changing the time-step;

3) Refine the time-step to the desired value, and run for five fan revolutions to establish high-order metrics such as

8

pressure fluctuations for acoustics. At this stage, any slope limiter used thus far is turned off, and the blended upwind-biased/centered left/right state reconstructions for the convective numerical flux are turned on;

4) Begin data collection for flow-field averaging over 10 fan revolutions.

The averaging procedure mimics that employed for the experimental dataset. Mean flow quantities are obtained at the hot-wire station 1 (Fig. 2a) by averaging over the 220 blade-passage sub-ensembles that are available in each numerical dataset that is obtained in this manner. Instantaneous fluctuations are then computed by subtracting this averaged flow-field from the full instantaneous dataset, and root-mean-square (RMS) values are computed by again taking the sub-ensemble average of this dataset.

The baseline time-step was chosen such that there would be at least 50 points-per-period (PPP) for acoustic waves of frequency corresponding to BPF_2. Additionally, an integer number of time-steps per blade pass was selected, so as to avoid having to perform an intermediate interpolation step to prevent aliasing errors from averaging of solution samples that do not map to the same rotor position. This resulted in a baseline number of time-steps per fan revolution of $T_{rev}^n = 98 \times 22 = 2156$.

A. Sensitivity Studies

In this section, several sensitivity studies to grid refinement level, time-step and turbulence model used for closure of the URANS equations will be assessed for the low-speed regime of the SDT fan stage. Table 1 summarizes the variations simulated within each sub-study, where R_f is the grid refinement factor applied in each (j, k, l) parametric direction and T_{rev}^n stands for the number of time-steps per fan revolution. All simulations performed in the context of the grid and time-step sensitivity studies were performed using the initialization procedure described at the start of Sec. IV. In regards to the turbulence model sensitivity cases, only the SA and SA-RC-QCR were run using this strategy. Other SA turbulence model variants were initialized using the flow-field solution resulting from the SA case, and allowed to run for a minimum of four fan revolutions before data collection for flow-field averaging began.

Table 1   Summary of sensitivity studies performed in the present work.

Scope	Variants	Comments
Grid Sensitivity	Coarse: $R_f = 0.8$ **Medium: $R_f = 1.0$** Fine: $R_f = 1.25$	URANS + SA, $T_{rev}^n = 2156$
Time-step Sensitivity	Coarse: $T_{rev}^n = 1078$ **Medium: $T_{rev}^n = 2156$** Fine: $T_{rev}^n = 3234$	URANS + SA, $R_f = 1.0$
Turbulence Model Sensitivity	**SA** SA-RC SA-QCR SA-RC-QCR SA-CC	URANS, $R_f = 1.0$, $T_{rev}^n = 2156$

1. Grid Refinement Study

Solution sensitivity to grid refinement was assessed using a family of grids that has been consistently refined in all three parametric block directions, with an incremental refinement factor of 1.25. This study was performed at the low-speed regime for URANS only, using the SA turbulence model and a time-step corresponding to $T_{rev}^n = 2156$. The choice of turbulence model closure will become clear in Sec. IV.A.3.

Total and azimuthal grid point counts are presented in Table 2. Special care was taken to avoid aliasing duct modes, where grid points act as individual fan or stator blades (as discussed in [16]), by setting the azimuthal cell counts to multiples of the rotor or OGV blade counts (22 and 54, respectively) depending on the location of the grid relative to

Table 2 Metrics for the family of grids created for the grid refinement study.

Refinement Level		Coarse	Medium	Fine
Refinement Ratio R_f		0.8	1.0	1.25
Viscous Wall Spacing (m)		6.25×10^{-6}	5.0×10^{-6}	4.0×10^{-6}
Grid Point Counts	Total Points	236,500,101	447,776,278	801,581,618
	Blanked Points	12,930,218	25,008,354	44,924,390
	Fringe Points	24,308,381	37,709,931	50,964,856
	Solution Points	199,261,502	385,057,993	705,692,372
Azimuthal Point Counts N_ϕ	Nacelle	529	661	837
	Inlet	419	506	639
	Rotor	639	793	969
	Interstage	639	793	991
	OGV	1,189	1,297	1,567
	OGV Exit	811	973	1,243
	Exhaust †	441	551	703

† The exhaust grid shown in Fig. 4a has been split in several locations along the radial direction, to allow for a radially-increasing N_ϕ. This was done to minimize the number of grid points while respecting the 15 PPW requirement for BPF_2 on the low-speed regime for the medium grid level.

these components. The viscous wall spacing is set on the medium grid level to a value of 5.0×10^{-6} m, corresponding to a y^+ value below 5.0 almost everywhere, thus allowing integration to occur all the way to the wall without any special near-wall treatment.

Table 3 presents the results of the grid refinement study in terms of fan stage performance metrics, compared to data that is available from the SDT campaign [4]. Overall these macro metrics show excellent agreement with experimental data. Interestingly, the mass flow rate got further from the experimental value as the grid resolution increased. Total pressure and temperature ratios were computed from the corresponding mass-averaged quantities measured at the nacelle exit, normalized by free-stream values. A 0.1 % to 0.6 % difference with experimental data is observed throughout all grids.

Sensitivity of the blade surface flow-field to the grid refinement level was also assessed. This analysis is shown in

Table 3 Performance metrics results for the grid refinement study.

Case	Metric		
	Mass Flow Rate kg/s (% Δ) †	**Total Pressure Ratio (% Δ)**	**Total Temperature Ratio (% Δ)**
SDT Data	26.535 (−)	1.154 (−)	1.049 (−)
Coarse	26.768 (+0.84)	1.160 (+0.52)	1.050 (+0.10)
Medium	26.779 (+0.92)	1.160 (+0.52)	1.050 (+0.10)
Fine	26.840 (+1.15)	1.161 (+0.61)	1.050 (+0.10)

† % Δ Difference between numerical result and SDT data.

Fig. 7. The center column composed of 4 images (labeled *Medium Grid*) shows blade surface contours of pressure (top) and axial skin friction (bottom) coefficients (C_p and $C_{f,x}$, respectively), for both the suction and pressure sides of the fan blade. These results were taken from the averaged flow-field of the case run on the medium grid level. Figure 7i indicates the flow re-attachment boundary as a dashed line, showing the leading edge part of the suction side of the blade experiences separated flow. The left and right columns (labeled Δ (*Medium − Coarse*) and Δ (*Fine − Medium*), respectively) show differences in these variables between successive grid refinements. Overall, little sensitivity to grid resolution is observed on the blade surface, apart from some localized differences in the suction side near the leading edge (for C_p) and near the hub, in the mid-chord region (for $C_{f,x}$). C_p and $C_{f,x}$ profiles along the blade chord were also analyzed at different spanwise stations (illustrated in each figure), and are presented in Appendix A. These profiles support the same conclusions drawn from the surface contours, showing only slight variations in C_p at the blade trailing edge. Axial skin friction coefficient shows larger grid sensitivity, especially on the suction side of the blade. While the pressure side of the blade shows signs of grid convergence between the medium and fine grid levels, the suction side profiles suggest that a larger number of grid points would be necessary to achieve the same behavior.
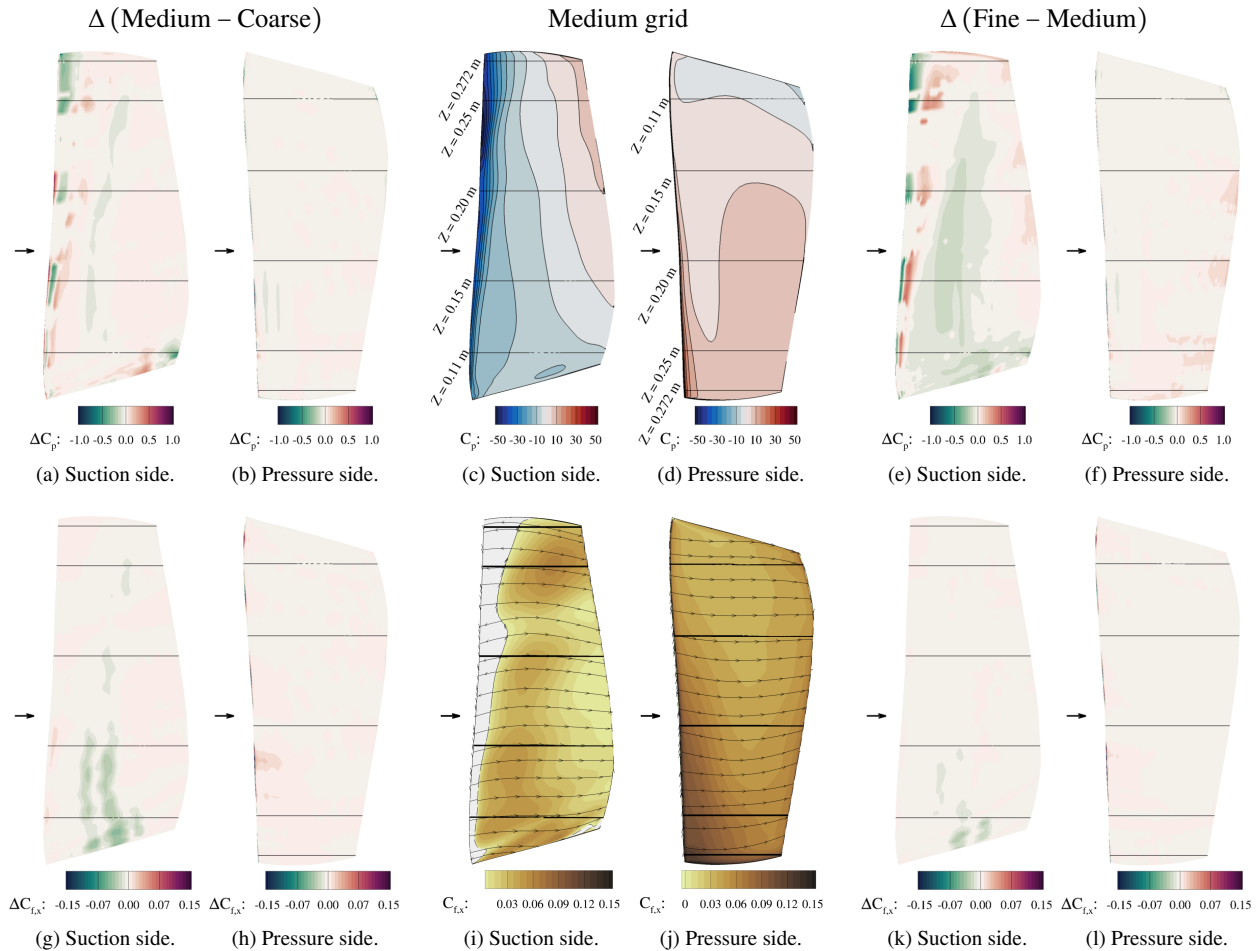
Fig. 7 Blade surface contours of pressure coefficient C_p (top row) and axial skin friction coefficient $C_{f,x}$ (bottom row). Medium grid results shown on the center column (Figs. 7c, 7d, 7i and 7j). Flow re-attachment boundary shown as a dashed (−−) line in Fig. 7i. Left and right columns show the difference between successive grid refinement levels (medium/coarse and fine/medium, respectively). Horizontal lines indicate where the profiles shown in Appendix A are taken.

Figure 8 compares the mean velocity profiles - axial (U), azimuthal (V_θ) and radial (V_r) - extracted along different radial lines at the hot-wire station 1 plane. The location of these lines is illustrated in Figs. 8a through 8c, which show these mean velocity contours on the medium grid level for reference. Both hot-wire and LDV data are added for reference. Although a more thorough discussion on a comparison between numerical and experimental data is deferred

to Sec. IV.B, differences in mean velocity profiles across all grid refinement levels is hardly noticeable.

The results presented in this section support the idea that, when it comes to stage performance metrics and averaged flow quantities, not much is gained from refining the grid past the coarse grid level used in the present work. However, the 15 PPW grid spacing requirement for BPF_2 based on the simplified acoustic analysis discussed in Sec. III.D is not satisfied on the coarse grid level. As such, in view of the acoustic analysis that is to be published in Part II of this study, all subsequent simulations were conducted using the medium grid level.

2. Time-step Refinement Study

A time-step refinement study was conducted on the medium grid level using URANS with the SA turbulence model closure at the low-speed regime. Three time-steps were analyzed, corresponding to a number of time-steps per fan revolution (T_{rev}^n) of 1078, 2156 and 3234. These correspond to the minimum time-step required to resolve 50 PPP (points-per-period) of BPF_1, BPF_2 and BPF_3, respectively.

Sensitivity of averaged flow quantities to the time-step was assessed via the same metrics presented in the previous section regarding the grid refinement study. Almost no sensitivity was observed in terms of stage performance metrics. The same is true regarding the blade surface flow-field. For brevity, only results pertaining to the hot-wire station 1 averaged flow-field are included in the manuscript. These are presented in Fig. 9. Some sensitivity to the time-step is observed, especially towards the casing ($r/R > 0.8$), where the blade tip vortices play a strong effect downstream of the rotor (Figs. 9d, 9h, 9i and 9l). Nonetheless, the medium and fine time-step results show good agreement with each other, whereas some visible differences are present relative to the coarse time-step profiles in certain regions (see Fig. 9l). While these differences alone may not be sufficient to justify the added cost of the medium time-step relative to the coarse one, only the former guarantees 50 PPP for BPF_2. For this reason, the medium time-step ($T_{rev}^n = 2156$) was chosen for the remainder of this work.

3. Turbulence Model Sensitivity Study

A final sensitivity study was performed on the turbulence model closure applied to the time-dependent RANS system of equations. The models tested in this work include: SA, SA-RC, SA-QCR, SA-RC-QCR and SA-CC. Additional details regarding these closures were provided in Sec. III.A.

One of the first test runs performed in the course of developing best-practices for this case utilized the SA-RC-QCR closure. Post-processing of the time-dependent pressure field around the fan stage indicated the presence of high-amplitude acoustic tones in the power spectral density (PSD) spectra that did not match any harmonic of the BPF. This suggested the presence of large-scale flow features that were not present in the experiment. To investigate the issue further, slices of the instantaneous axial velocity at the hot-wire station 1 axial location ($x = 0.1016$ m) were compared with the SDT data. These are shown in Fig. 10 for all model closures tested. Comparing Figs. 10a and 10d, corresponding to the SDT data and the SA-RC-QCR variant, shows the presence of spurious vortices distributed around the casing, without a clear repeating pattern. The interaction of these vortices with the OGVs located downstream was the likely cause for the spurious tones observed in the preliminary PSD spectra. The SA-RC and SA-QCR variants were then tested separately, in addition to the plain SA model, to understand which of these corrections was responsible for the irregular vortical structures appearing near the casing. These are shown in Figs. 10b, 10c and 10e, respectively. The contours suggest that the RC correction introduces irregular vortical structures that do not repeat on a *per-blade-pass* basis. The pattern emerging from the QCR correction applied to the SA model shows more regularity, but appears to overpredict the thickness of the tip vortex boundary layer region. The plain SA model shows the best agreement with the experimental instantaneous flow-field, with no irregular vortical structures present downstream of the fan. However, the casing boundary layer thickness is still overpredicted. Finally, the SA-CC variant was also tested, given its improved compressible mixing layer behavior for the exhaust region, but the same irregular vortical stuctures appear in the interstage, suggesting the flow-field in this region is highly sensitive to these corrections. Since any nonuniformly-repeating vortices interacting with the downstream OGVs will produce acoustic tones at frequencies other than BPF harmonics, the plain SA turbulence model was selected for the production runs.

To see if these irregular flow features present in the SA-RC, SA-CC and SA-RC-QCR turbulence model variants could be understood by looking at the blade surface flow-field, contours of surface C_p and $C_{f,x}$ were created for all model variants. Figure 11 presents those corresponding to the SA (top row) and SA-RC-QCR (bottom row) variants. Only these two are shown, corresponding to the closure used in this work and that used as best-practice in typical LAVA solver applications, since these are representative of the trends followed by the remaining variants. Overall, the flow topology appears similar between the two. The SA variant shows a stronger suction peak towards the edge of the blade
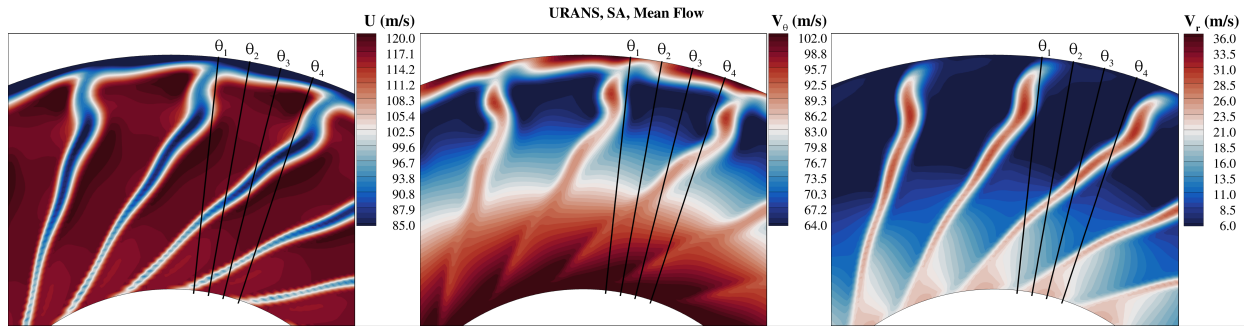
(a) U, medium grid.

(b) V_θ, medium grid.

(c) V_r, medium grid.
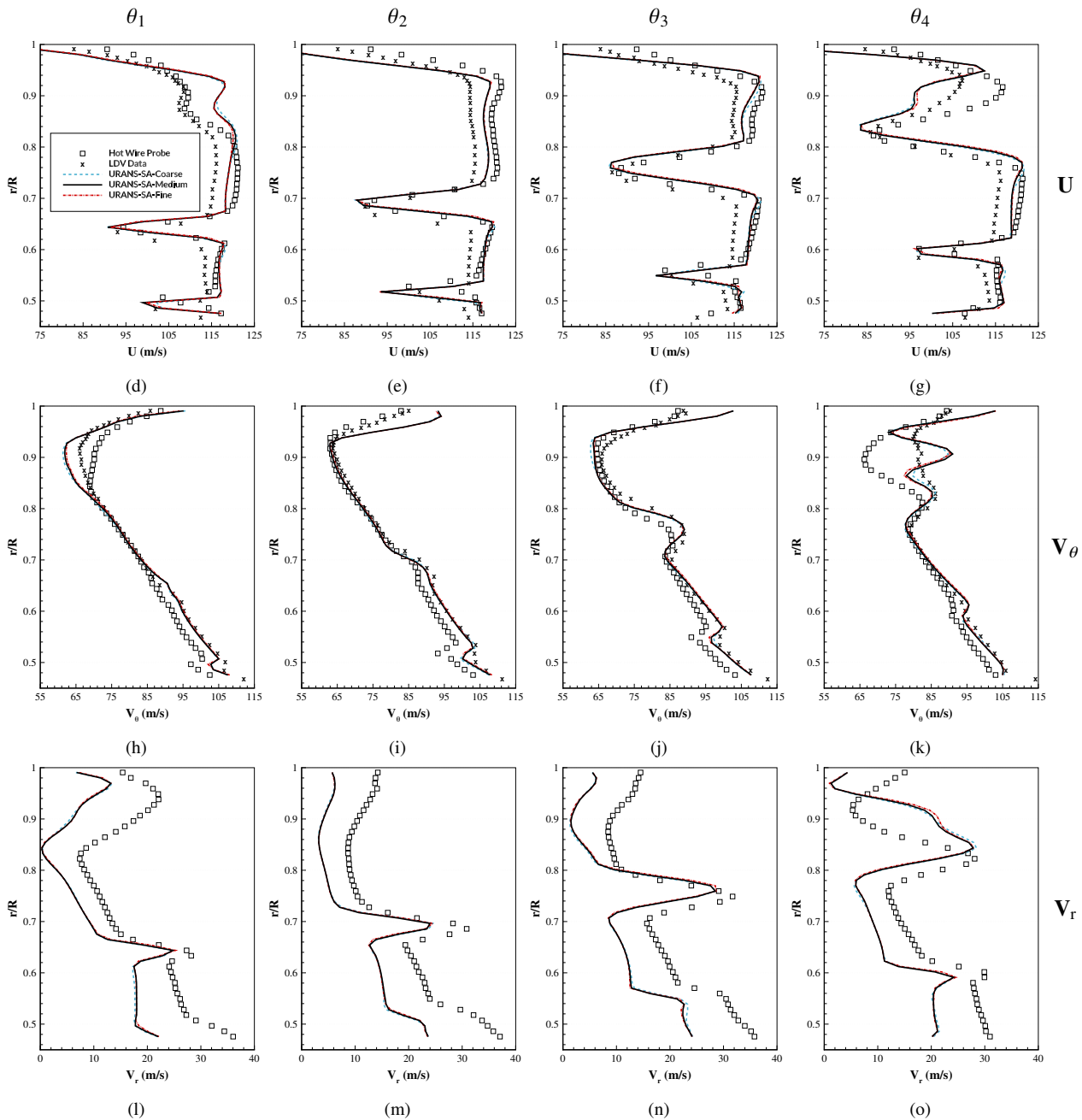
(d)

(e)

(f)

(g)

(h)

(i)

(j)

(k)

(l)

(m)

(n)

(o)

Fig. 8 Grid refinement study - mean axial, azimuthal and radial velocity profiles at hot-wire station 1.
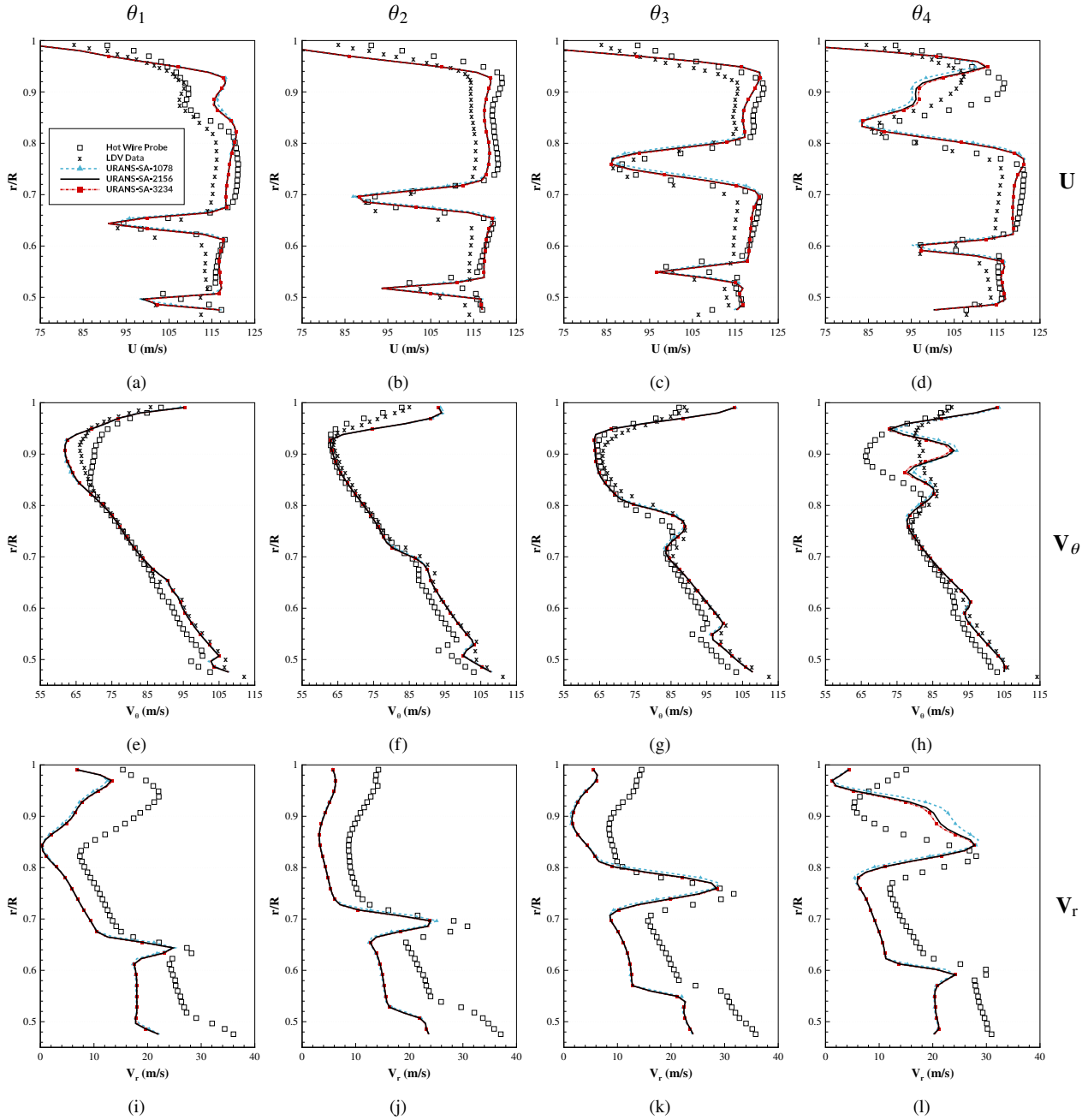
Fig. 9 **Time-step refinement study - mean axial, azimuthal and radial velocity profiles at hot-wire station 1.**

relative to the SA-RC-QCR case, while the ensuing pressure recovery occurs at about the same chord-length. This results in a stronger adverse pressure gradient for the SA model near the casing. However, as indicated by Figs. 11c and 11g, that does not delay flow re-attachment on the suction side of the blade (the flow re-attachment boundary is indicated in dashed −− lines). The most apparent difference between the two models occurs in the flow near the trailing edge at 20 % to 55 % span, as the flow separates in the SA-RC-QCR model, in contrast to the SA variant. Given the distance between this flow separation region and the blade tip, downstream of which the spurious vortical structures appear at the hot-wire probe station 1, it is unlikely to be the reason for their appearance. Despite not being shown, the observations listed here for the SA model also apply for the SA-QCR and SA-CC variants, while the flow topology of the SA-RC model follows that of the SA-RC-QCR variant closely. Finally, chordwise profiles of these coefficients were

(a) SDT data.

(b) SA-RC variant.

(c) SA-QCR variant.

(d) SA-RC-QCR variant.

(e) SA.

(f) SA-CC variant.
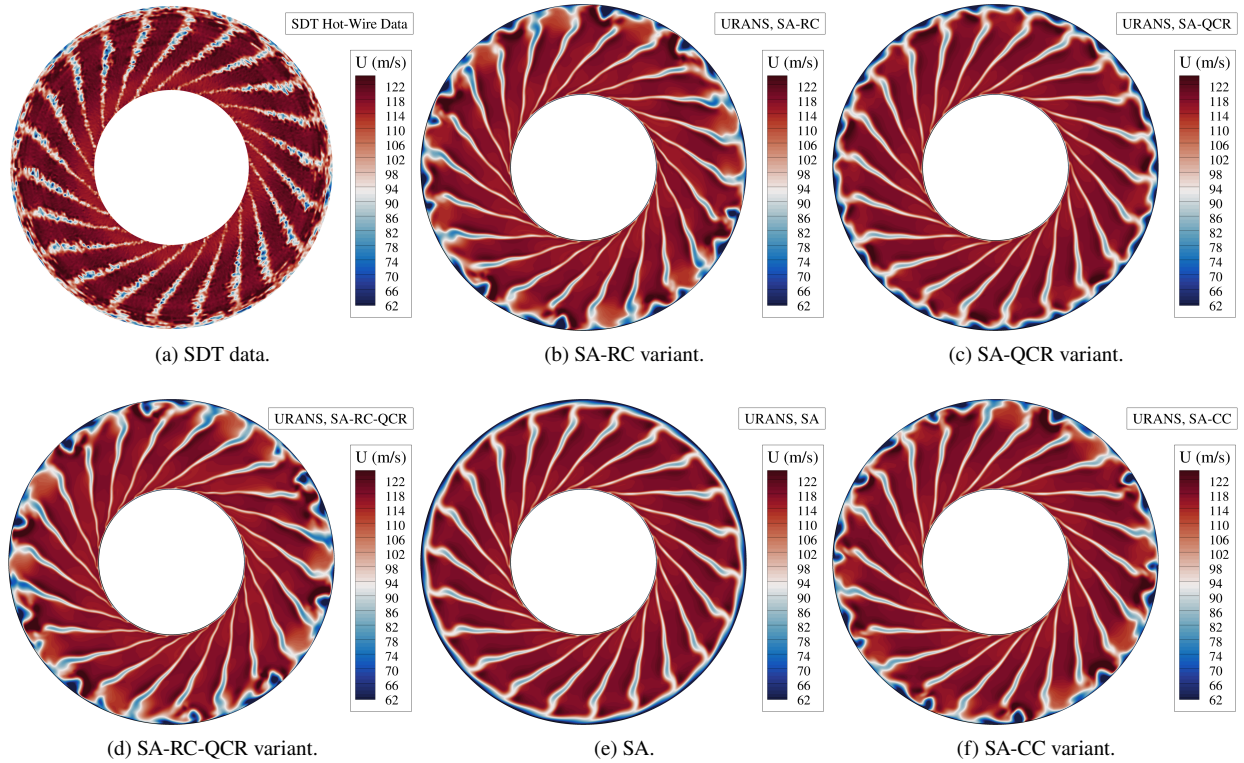
Fig. 10 Turbulence model closure study - instantaneous axial velocity contours at hot-wire station 1.

also extracted at different spanwise sections (those indicated in Fig. 7c) for a more quantitative comparison across turbulence model variants. These are included in Appendix B. These observations based on the contours are supported by the quantitative chordwise profile extractions. Two different trends can be observed to develop in the axial skin friction coefficient profiles. Interestingly, the SA, SA-QCR and SA-CC variants have a similar behavior, with no flow separation towards the trailing edge at the Z = 0.15 m profile, whereas the SA-RC and SA-RC-QCR closures form the other distinct trend observed in $C_{f,x}$.

The mean (Figs. 12 and 13) and root-mean-square velocity fluctuations (Figs. 14 and 15) were also assessed and compared with the SDT data taken at the hot-wire station 1 location, so as to establish which model produced results closer to experiment. The SA and SA-RC-QCR variants were chosen to represent the two distinct trends pointed out earlier. The mean axial velocity contours shown in Fig. 12 (left column) show that the SA-RC-QCR variant predicts a significantly thicker casing boundary layer, resulting from the presence of the spurious vortices in this region (see Fig. 10d). The SA results show closer agreement with the SDT data, albeit with a slower velocity recovery away from the wall. Azimuthal (center column) and radial (right column) contours again indicate a closer agreement with the SDT data when using the baseline SA model. Both models, however, seem to overpredict the azimuthal velocity near the hub and underpredict the radial velocity everywhere. A qualitative comparison of these results along different radial lines (shown in Fig. 8a) is presented in Fig. 13. Overall, good agreement with the experimental data is found for the mean axial velocity profiles (top row), with the numerical results lying between the two experimental datasets taken from the hot-wire data and the LDV measurements. The main exception to this trend occurs towards the casing ($r/R > 0.8$). In this region not only is there more sensitivity to the model closure used (resulting in the same two distinct trends observed), but also the models fail to capture the blade wake behavior captured by profiles θ_1 and θ_4. Similar observations apply to the mean azimuthal velocity profiles (middle row), showing excellent agreement with the LDV data everywhere except the blade wakes near the casing. It is unclear why the hot-wire azimuthal velocity data in Fig. 13h fails to capture the blade wake at r/R between 0.7 and 0.8, but both LDV and numerical results clearly show this local increase. The mean radial velocity profiles (bottom row), on the other hand, show a constant underprediction of this velocity component everywhere, independent of the turbulent closure used. The HRLES model did not seem to fix this discrepancy (as will be seen in Sec. IV.B), but the trend has been observed previously in past studies on the SDT
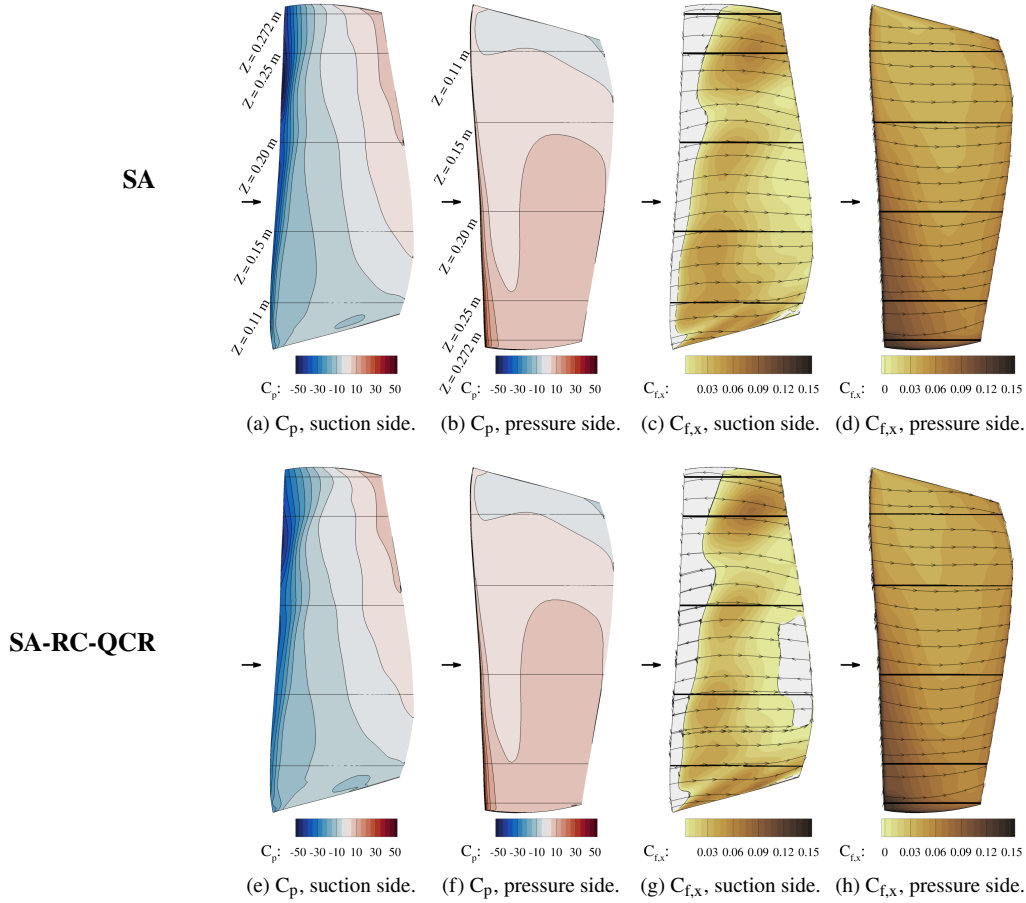
15

SA

(a) C_p, suction side.   (b) C_p, pressure side.   (c) $C_{f,x}$, suction side.   (d) $C_{f,x}$, pressure side.

SA-RC-QCR

(e) C_p, suction side.   (f) C_p, pressure side.   (g) $C_{f,x}$, suction side.   (h) $C_{f,x}$, pressure side.

Fig. 11   Blade surface contours of pressure (C_p) and axial skin friction ($C_{f,x}$) coefficients for the SA and SA-RC-QCR turbulence model variants. Solution data taken from the averaged flow-field.

[13].

A similar comparison between the numerical results for these two turbulence model closures and the SDT data regarding the root-mean-square of the velocity fluctuations is provided in Figs. 14 and 15. It was observed that the fluctuations computed via the method outlined at the start of Sec. IV were close to zero for the SA turbulence model. Essentially, the phase-locked mean velocity field was identical to the instantaneous velocity field, as the model tends to supress fluctuations. For this reason, the velocity fluctuations for this model were estimated from the turbulent kinetic energy (TKE), which may be estimated in the SA model using certain assumptions. Firstly, equilibrium between turbulence dissipation and production is assumed. Then, one uses the definition of the turbulent viscosity v_T from the $k - \varepsilon$ turbulence model and the Bradshaw's hypothesis to express the TKE as a function of the strain rate tensor and the turbulent viscosity as $k_T = v_T \left\| \overline{S_{ij}} \right\| / \sqrt{C_\mu}$. Finally, all three velocity fluctuation components are assumed identical, leading to an approximation of the turbulent velocity field as $u' = (2/3 k_T)^{1/2}$. The velocity field shown in Fig. 14d was obtained following this procedure. While none of the models are expected to capture velocity fluctuations accurately using URANS, the fan blade wakes were observed to have similar values in magnitude relative to the SDT data for the baseline SA case. The SA-RC-QCR variant not only underpredicts velocity fluctuations in this region, but also overpredicts the near-casing turbulent content, likely an effect of the spurious vortical structures noted earlier.

A quantitative comparison is provided in Fig. 15 for all turbulence model variants tested and the SDT data, following the same analysis conducted for the mean flow. The three velocity profiles plotted for the SA variant are identical, but vary between azimuthal stations (θ_1 through θ_4). Surprisingly, the SA model fluctuations estimated from the TKE show better-than-expected agreement with the SDT data, considering they were predicted with URANS, especially away from the casing. The fan blade wakes present a strange drop in fluctuations at their center, possibly due to the wake-following
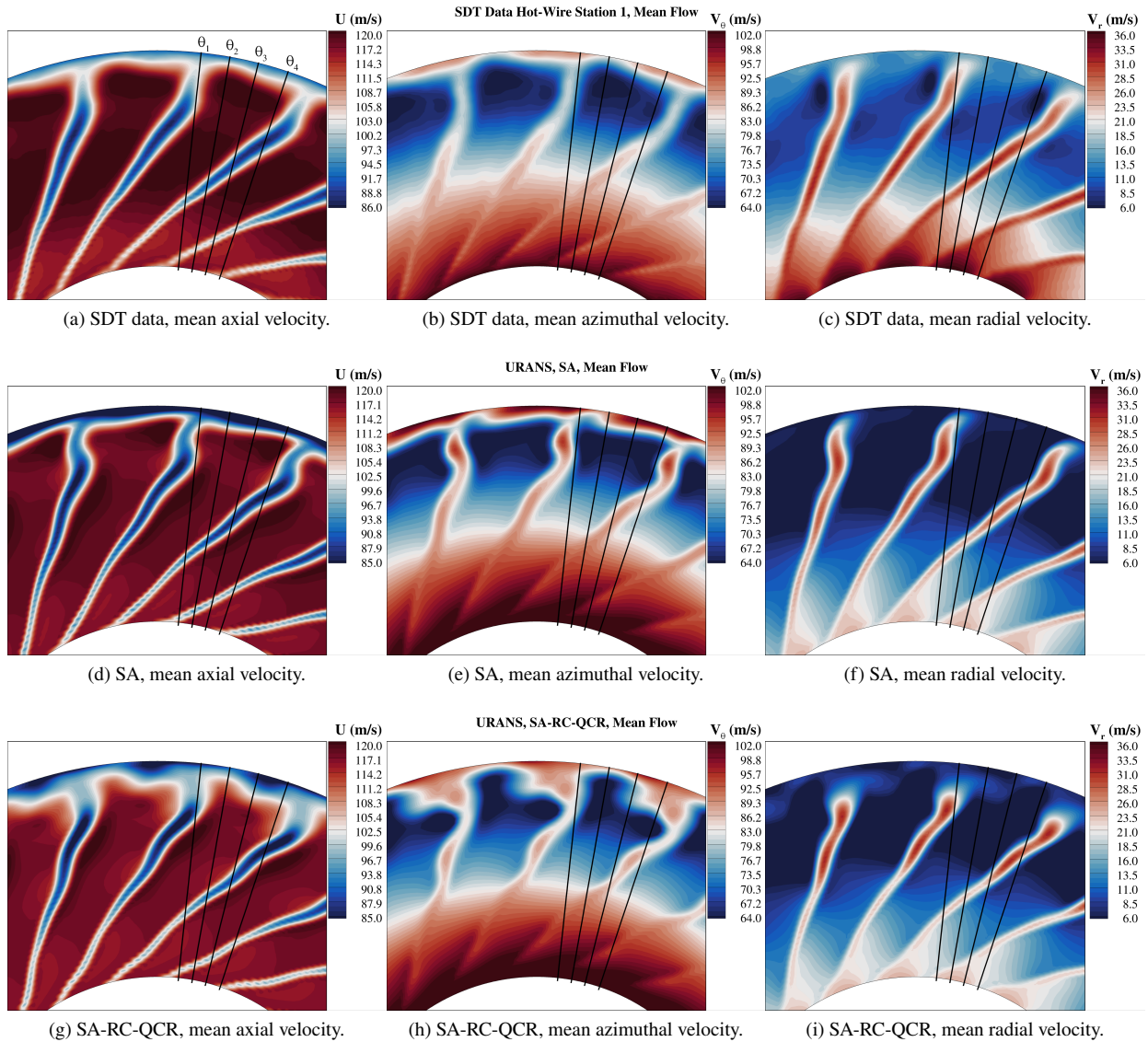
(a) SDT data, mean axial velocity.

(b) SDT data, mean azimuthal velocity.

(c) SDT data, mean radial velocity.

(d) SA, mean axial velocity.

(e) SA, mean azimuthal velocity.

(f) SA, mean radial velocity.

(g) SA-RC-QCR, mean axial velocity.

(h) SA-RC-QCR, mean azimuthal velocity.

(i) SA-RC-QCR, mean radial velocity.

Fig. 12   Mean velocity contours at hot-wire station 1 from the SDT data (top row) and URANS results from two turbulence model variants, namely SA (center row) and SA-RC-QCR (bottom row).

grid blocks added downstream of each blade. This will be assessed in the future with a grid that replaces these blocks with a more uniform circumferentially-revolving grid in this region. Significant sensitivity in these velocity fluctuation components is observed across different turbulence model closures, with the SA-RC-QCR variant doing a good job at predicting the local spike near blade wake regions, albeit at a much lower magnitude relative to the experimental data. Velocity fluctuations estimated from the TKE were also extracted from the SA-RC-QCR case, and are plotted in green. These show close agreement with the SA results, except near the casing whenever blade wakes are present. Compared to the standard fluctuation computation method used for the remaining variants, the profiles estimated from the TKE show fluctuation magnitudes closer to the SDT data.
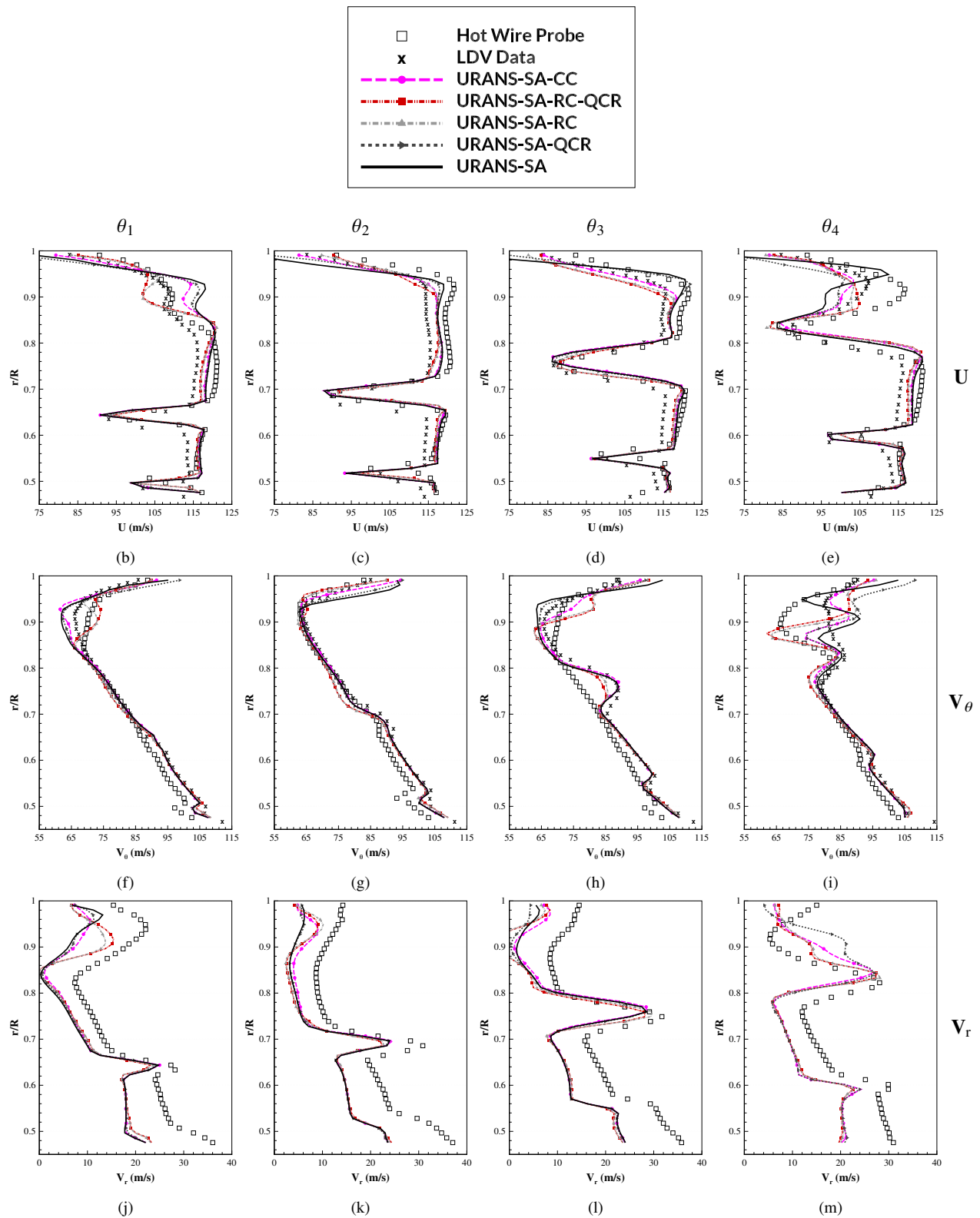
Fig. 13 Turbulence model sensitivity - mean axial, azimuthal and radial velocity profiles at hot-wire station 1. LDV data not available for radial velocity component V_r (bottom row).
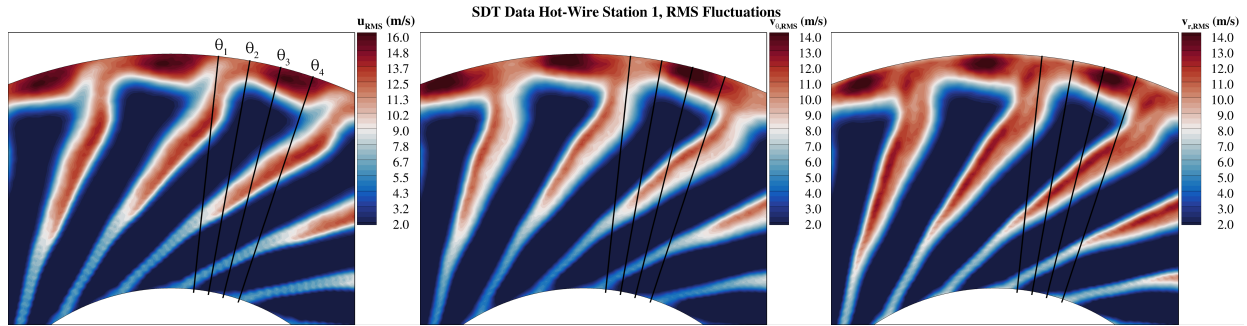
(a) SDT data, axial velocity fluctuations.

(b) SDT data, azimuthal velocity fluctuations.

(c) SDT data, radial velocity fluctuations.
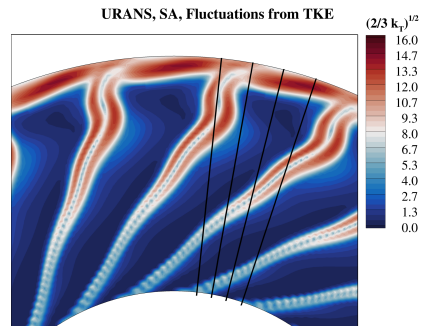
(d) SA, velocity fluctuations estimated from turbulent kinetic energy.
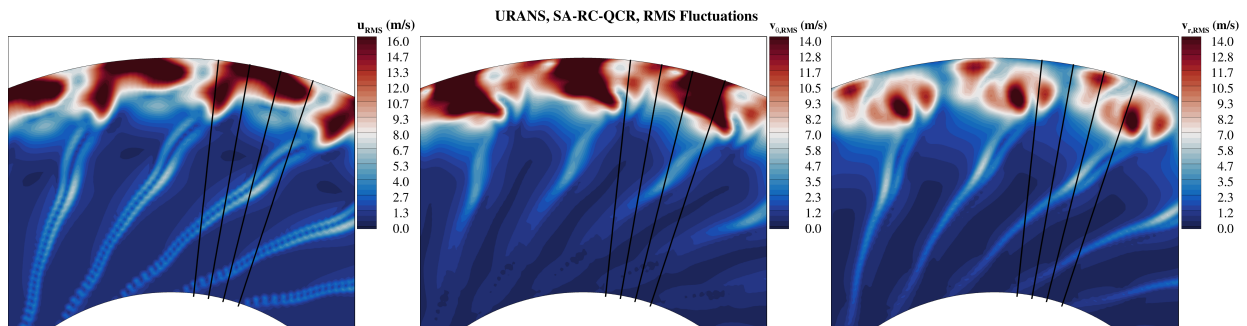
(e) SA-RC-QCR, axial velocity fluctuations.

(f) SA-RC-QCR, azimuthal velocity fluctuations.

(g) SA-RC-QCR, radial velocity fluctuations.

Fig. 14 Velocity fluctuation contours at hot-wire station 1 from the SDT data (top row) and URANS results from two turbulence model variants, namely SA (center row) and SA-RC-QCR (bottom row).
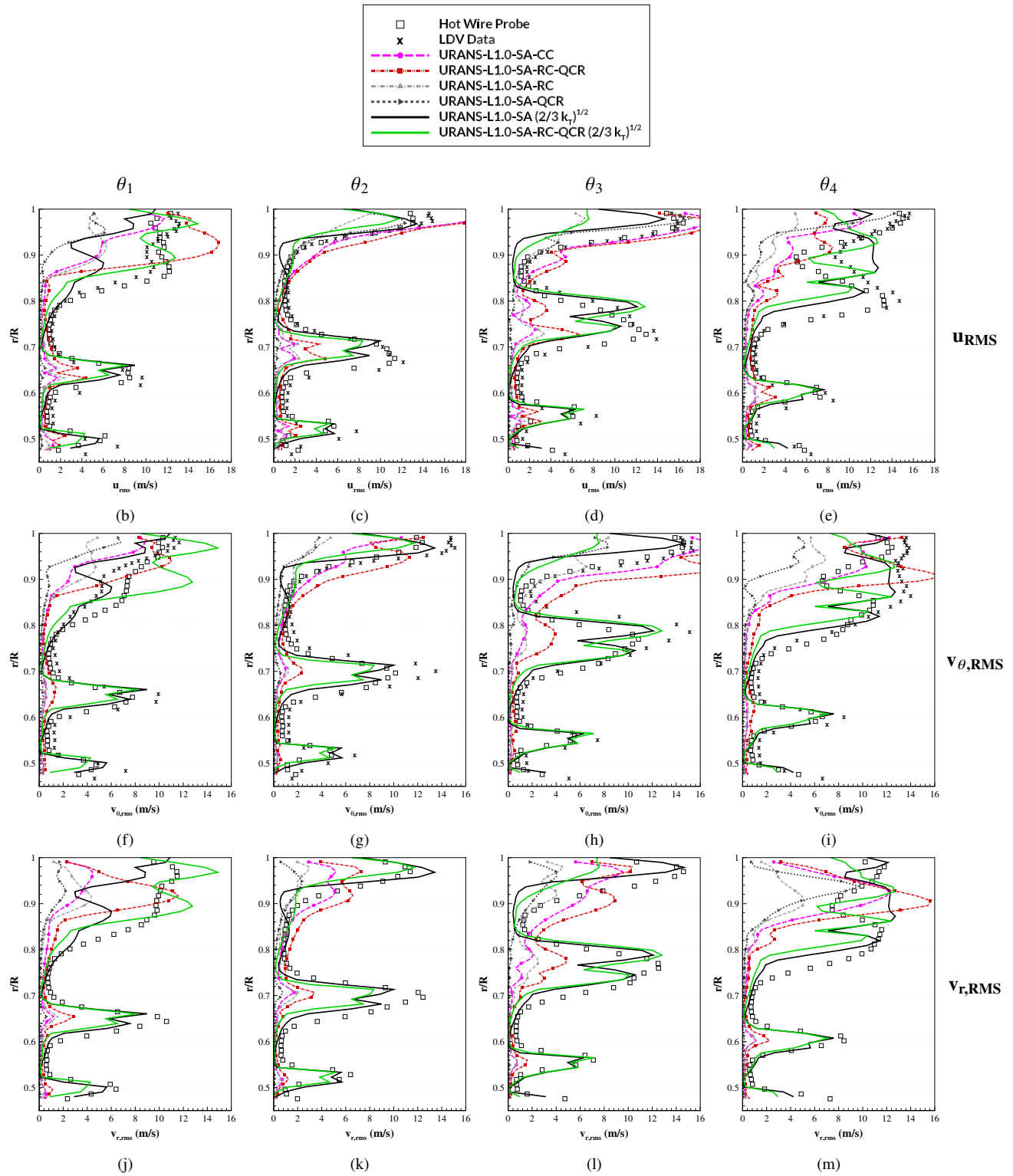
Fig. 15 Turbulence model sensitivity - RMS of axial, azimuthal and radial velocity fluctuations at hot-wire station 1. LDV data not available for radial velocity component V_r (bottom row).

B. Approach (Low-Speed) Condition

In this section, results for the low-speed regime are presented for both URANS and HRLES methods. The baseline SA turbulence model is used throughout these production runs in regions treated with URANS, as this was determined to be best practice in Sec. III.A. An extensive comparison with available experimental data is performed, and both methods are assessed in their capability to predict aerodynamic and turbulence quantities around the fan stage. The section starts with a showcase of flow visualizations to emphasize the main differences between both methods when it comes to resolving small-scale turbulence, which translates into a significant contrast in the acoustic signature predicted by each. Once the reader is familiarized with the flow-field, quantitative comparisons with experimental data are presented.

1. Low-Speed Regime - Qualitative Comparison of CFD Modeling Approach

Figure 16 shows slices of the mean and instantaneous axial velocity across the stage, taken from the experiment (top row) and the two methods (URANS on the top center row, HRLES on the bottom center). The bottom row shows a qualitative comparison of these velocity profiles extracted along the streamtrace plotted in Fig. 16a. Excellent agreement is observed between the SDT data and both methods upstream of the fan and OGV stages. Downstream of these components, HRLES lies on top of the experimental data until the nozzle exit, and then slowly begins overpredicting the mean axial velocity component. URANS overpredicts the nozzle exit peak, and then outperforms the HRLES case in this metric further downstream. Both radial and azimuthal velocity components closely follow the experimental data for both methods. From a qualitative point of view, Figs. 16c and 16e exemplify the capabilities of HRLES in predicting small-scale turbulent content, especially in the shear layer developing downstream of the nacelle trailing edge. Without these features, one cannot hope to predict broadband noise. Finally, Fig. 16g compares instantaneous velocity snapshots taken from the URANS and the HRLES runs. Upstream of the fan and OGV stages these are identical. On the downstream section, however, fine turbulent structures are clearly present in the HRLES flow-field, resulting from the scale-resolving nature of this method in regions treated with LES.

Figures 17 and 18 show slices of normalized vorticity magnitude along several axial stations and at a meridional plane. These images further emphasize the different character of the two approaches when it comes to their capability to resolve fine-grained turbulent structures. While URANS fails to capture most of the vorticity content present in the midsection between the hub and the casing downstream of the fan and OGV stages (notice the white streaks in the exhaust, showing the normalized vorticity values are less than 10, and the difference between Figs. 18c and 18f at the nozzle exit), HRLES exhibits vortical structures in this LES mode region with significantly larger amplitudes. Additionally, the vorticity in the shear layer starting at the nacelle trailing edge is larger and extends further downstream, as these vortices evolve and dissipate along the energy cascade.

A snapshot of the pressure derivative field is presented in Figs. 19a and 19b for both methods along a meridional plane. These allow for a visual and intuitive depiction of the sound wave pattern propagation around the fan stage. A clear difference between the two methods is apparent from these images. URANS lacks any of the small-scale pressure waves present in the shear layer, in contrast to the HRLES result. This again shows why URANS is only capable of predicting acoustic tones without the broadband component. The propagation of two distinct tones with different wavelengths is visible in the URANS result. The higher wavelength tone (propagating along the hub in the downstream direction) is associated with BPF_1, while the higher frequency one propagating along the sideline arc and onto the microphones (shown in Fig. 3) is associated with BPF_2. Comparison with the HRLES result also shows that URANS fails to capture any of the fore-propagating noise in the inlet, which is mostly broadband at this low-speed condition. This is because the BPF tone is cut-off (exponentially decaying) in the present rotor-stator configuration at subsonic fan tip speeds. Thus, it is expected that URANS significantly underpredicts the noise level at frequencies corresponding to BPF harmonics in the low-speed regime, especially at the lower sideline angles where the broadband fore-radiated noise from the inlet is more impactful.

Additional slices of the pressure derivative field along different axial stations are also presented in Fig. 20, with URANS and HRLES results shown on the top and bottom rows, respectively. URANS shows the propagation of pressure waves in well-defined spiral patterns correlated to the fan rotational speed. These patterns are no longer clearly identifiable in the HRLES simulation, since the broadband noise strongly disrupts the regularity of these features. Stronger amplitudes are also visibly noticeable in the HRLES results. The slice taken at the nacelle inlet emphasizes the broadband character of the noise in this region. Figure 20d also shows an interesting acoustic behavior. The outer region of the nacelle - showing noise that propagated from the exhaust, around the trailing edge and began traveling in the fore direction (given that the inlet rotor-locked tones are evanescent) - shows the spiral pattern characteristic of tonal noise. This indicates that noise originating from the nacelle trailing edge and traveling upstream is mainly tonal in nature.
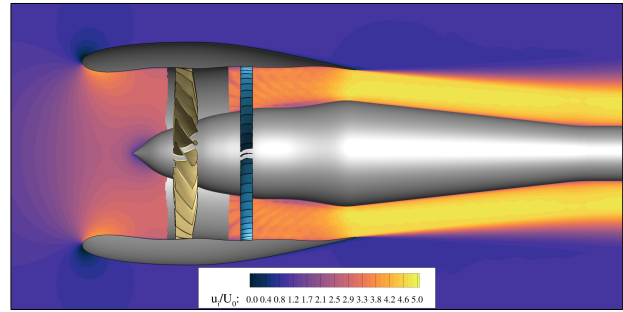
Finally, profiles of C_p and $C_{f,x}$ taken at several spanwise stations along the blade surface (those shown in Fig. 7) are included in Appendix C. The main differences observed between the two models occur near the hub and blade tip, where influence from the intersecting streamwise boundary layer is highest.
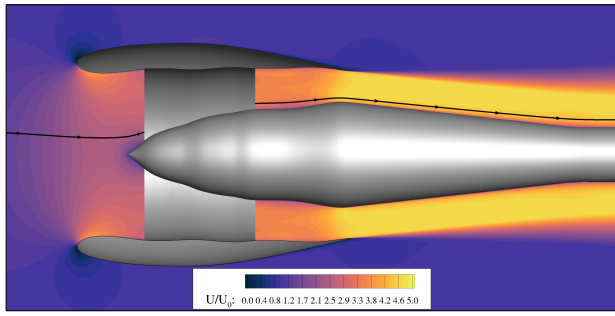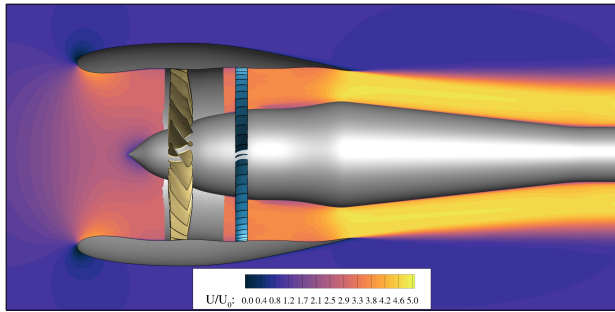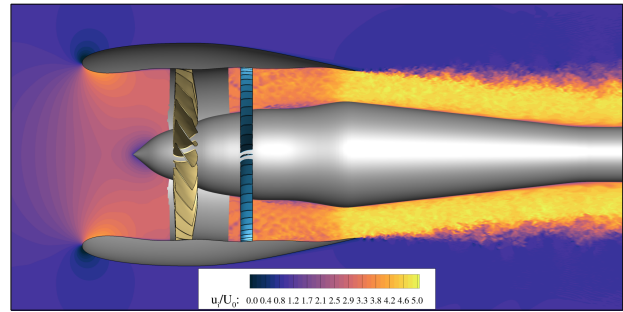
(a) SDT data, mean axial velocity.
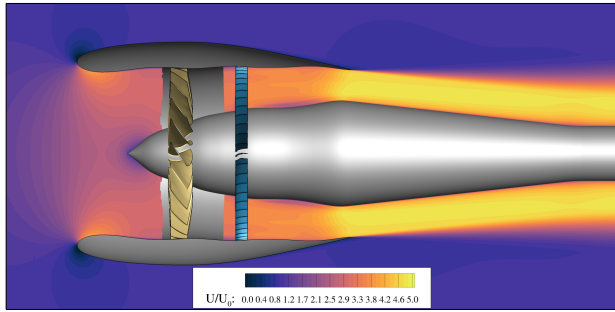
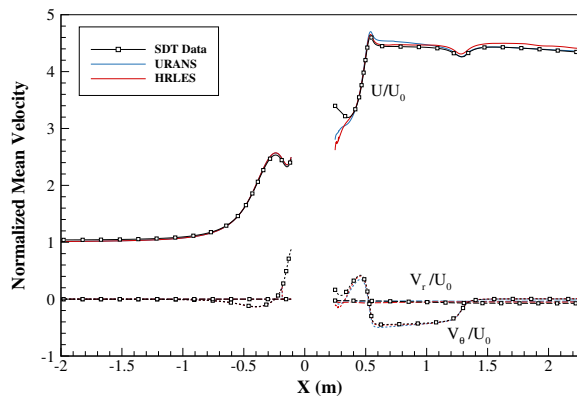(b) URANS (SA), mean axial velocity.
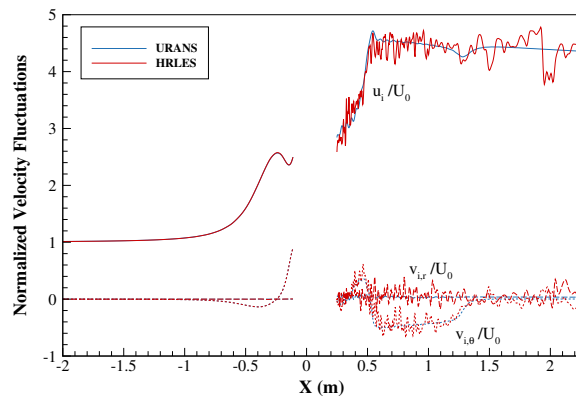

(c) URANS (SA), instantaneous axial velocity.

(d) HRLES, mean axial velocity.

(e) HRLES, instantaneous axial velocity.

(f) Mean velocity profiles along streamtrace.

(g) Instantaneous velocity profiles along streamtrace.

Fig. 16   Slices of mean (left column) and instantaneous (right column) axial velocity from SDT data (top row) and both URANS and HRLES results (top center and top bottom rows, respectively) at the low-speed regime. Comparison of mean (left) and instantaneous (right) velocity profiles along the streamtrace illustrated in Fig. 16a (bottom row).

(a) URANS (SA), normalized vorticity magnitude.

(b) HRLES, normalized vorticity magnitude.
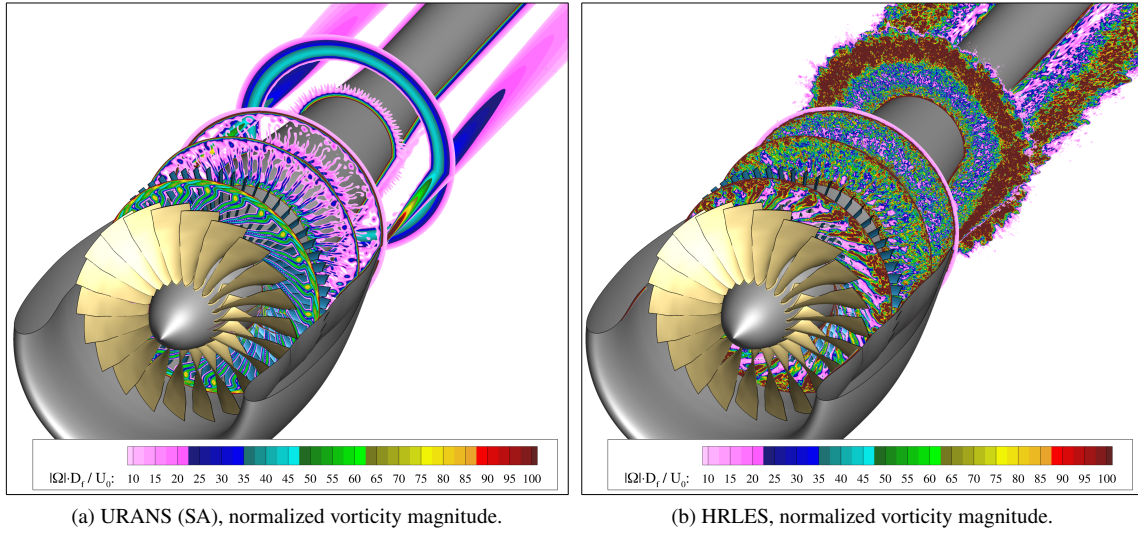
Fig. 17 Snapshots of vorticity magnitude normalized by the fan diameter D_f and freestream velocity U_0 for URANS (left) and HRLES (right) at the low-speed regime. Values below 10 were hidden for clarity.
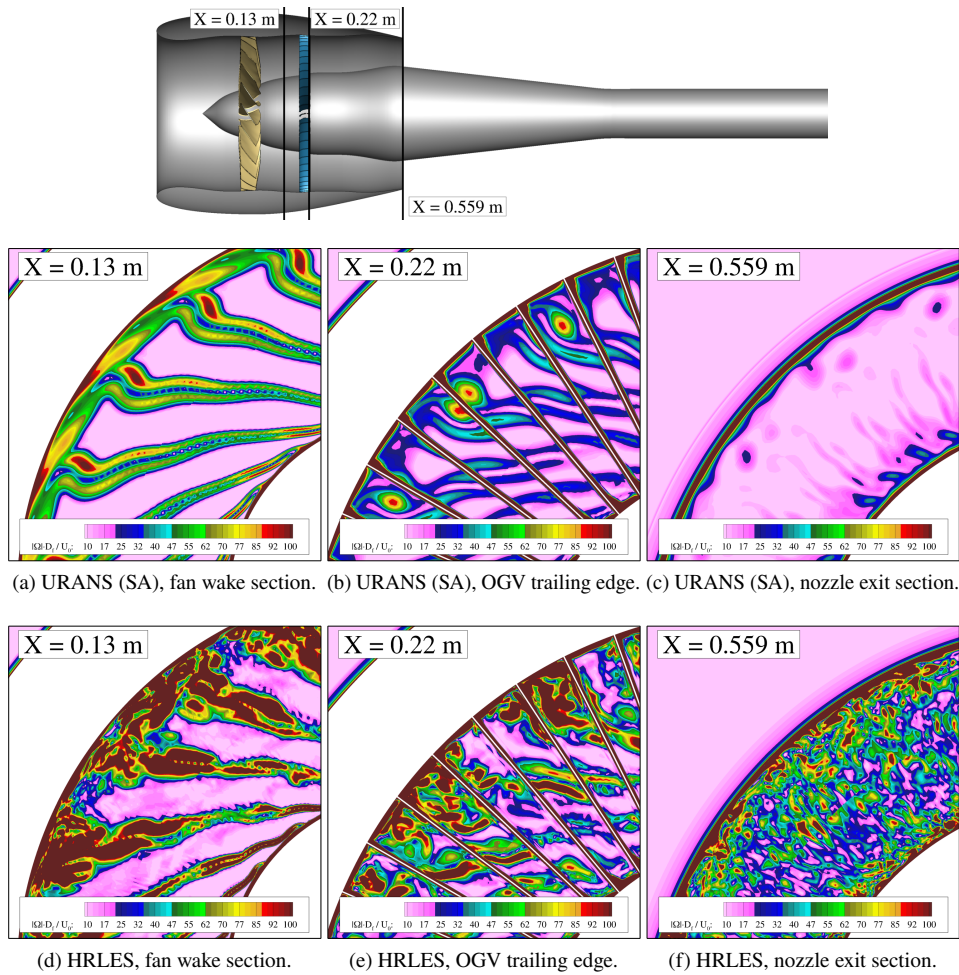

(a) URANS (SA), fan wake section. (b) URANS (SA), OGV trailing edge. (c) URANS (SA), nozzle exit section.

(d) HRLES, fan wake section. (e) HRLES, OGV trailing edge. (f) HRLES, nozzle exit section.

Fig. 18 Snapshots of vorticity magnitude normalized by the fan diameter D_f and freestream velocity U_0 at several stations inside the fan stage for URANS (top row) and HRLES (bottom row) at the low-speed regime.

24
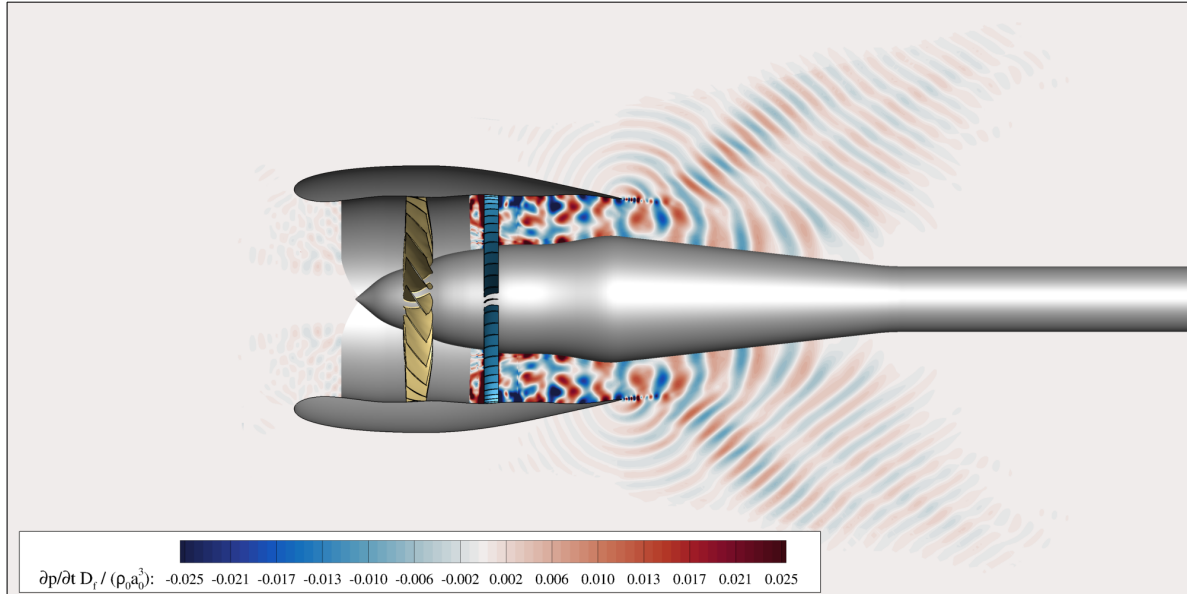
(a) URANS (SA), pressure waves pattern at a slice cutting through the fan stage.
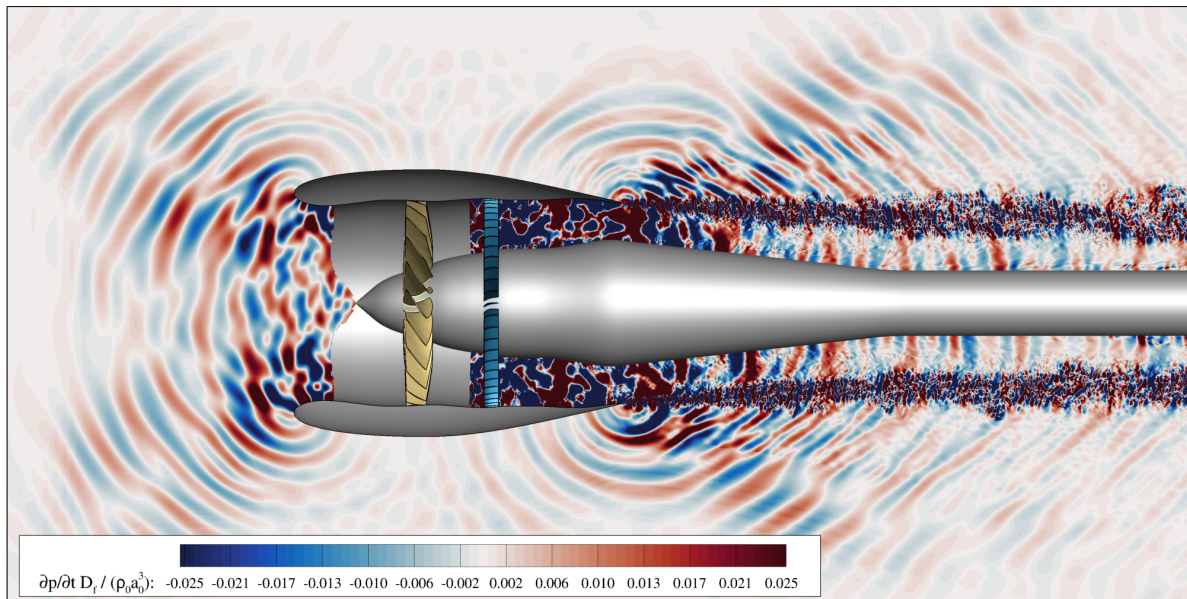
(b) HRLES, pressure waves pattern at a slice cutting through the fan stage.

Fig. 19   Snapshots of pressure time derivative normalized by the fan diameter D_f, freestream density ρ_0 and sound speed a_0 for URANS (top) and HRLES (bottom) at the low-speed regime.
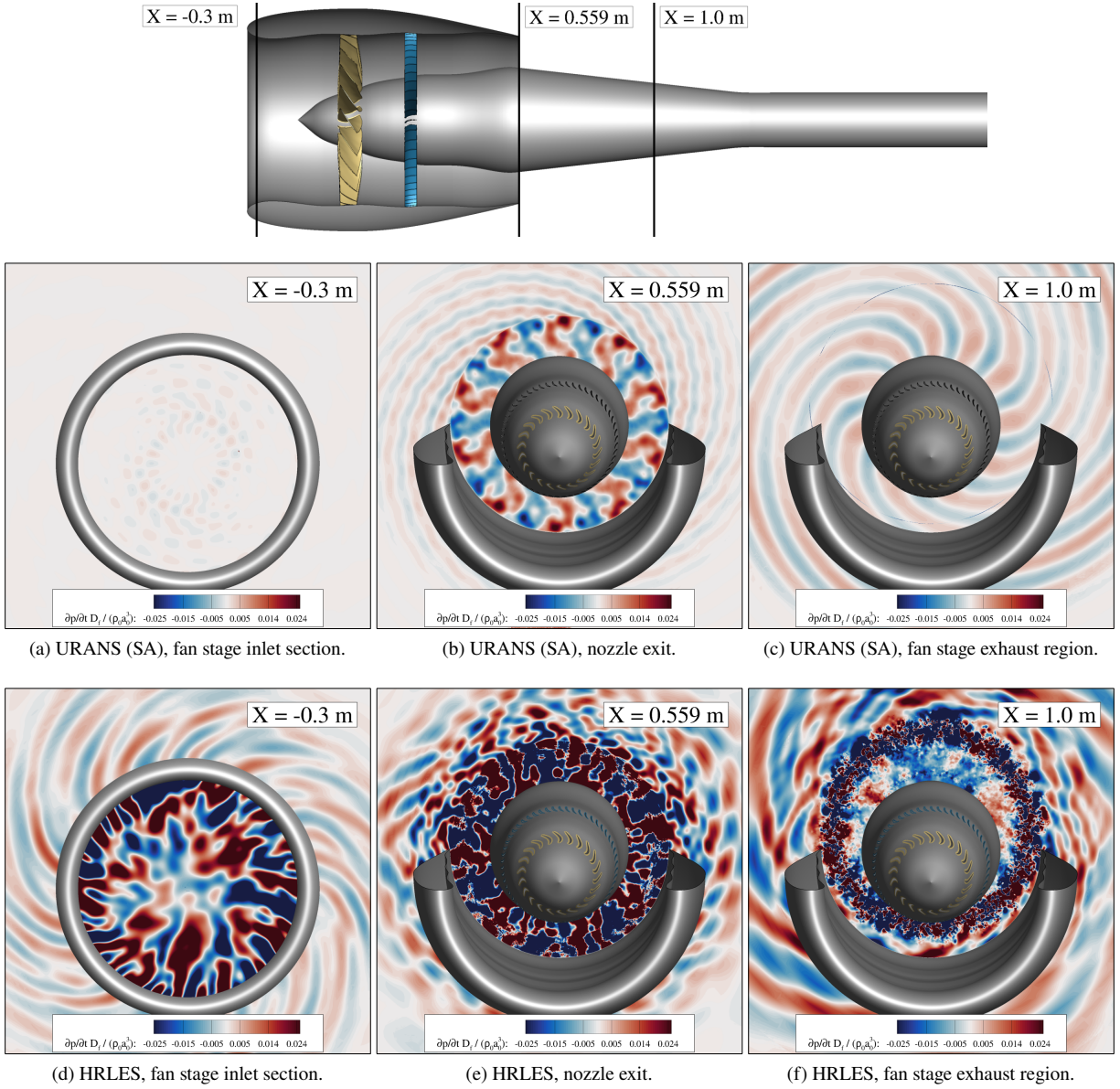
(a) URANS (SA), fan stage inlet section.

(b) URANS (SA), nozzle exit.

(c) URANS (SA), fan stage exhaust region.

(d) HRLES, fan stage inlet section.

(e) HRLES, nozzle exit.

(f) HRLES, fan stage exhaust region.

Fig. 20 Snapshots of pressure time derivative normalized by the fan diameter D_f and freestream density ρ_0 and sound speed a_0 at several axial stations for URANS (top row) and HRLES (bottom row) at the low-speed regime.

2. Low-Speed Regime - Validation with SDT Data

Key fan stage metrics predicted with URANS and hybrid RANS/LES are compared with the SDT data in Table 4. Mass flow rate, total pressure and total temperatures are measured at the nozzle exit section (last two quantities are mass-averaged) and their ratios calculated relative to freestream values. Excellent agreement is found on all metrics, with less than 1 % error relative to the experiment.

Table 4   Performance metrics results for the low-speed regime.

Case	Metric		
	Mass Flow Rate kg/s (% Δ) [†]	**Total Pressure Ratio (% Δ)**	**Total Temperature Ratio (% Δ)**
SDT Data [4]	26.535 (−)	1.154 (−)	1.049 (−)
URANS (SA)	26.779 (+0.92)	1.160 (+0.52)	1.050 (+0.10)
HRLES	26.780 (+0.92)	1.161 (+0.61)	1.050 (+0.10)

[†]   % Δ Difference between numerical result and SDT data.

Figure 21 shows the averaged velocity (top three rows) and RMS of velocity fluctuation (bottom three rows) components for the low-speed regime at hot-wire station 1. Overall good agreement is observed with the SDT data for both methods when it comes to the mean flow, with the exception of the radial velocity component which is underpredicted by both URANS and HRLES. Similar to previously published results, unsteady RANS predicts an S-shaped wake (visible in the mean axial velocity contour, Fig. 21b) while the HRLES wake closely resembles that of the experiment. On the other hand, the velocity deficit in the wakes is more accurately captured by URANS. The same is true for the azimuthal velocity component. In regards to the velocity fluctuations, only the component extracted from the TKE is plotted, since the SA model was used for these production runs. HRLES does a good job at locating where these fluctuations are highest at blade wakes and around the casing, but overpredicts their RMS average relative to the SDT data for the axial and azimuthal components. The radial component, on the other hand, is underpredicted, especially near the casing. The lack of a radial velocity component on the turbulent flow near the casing indicates that the turbulent structures forming in this region are not eddies with an X-aligned axis of rotation, as appears to be the case in the SDT dataset.

Figures 22 and 23 present the qualitative equivalent of Fig. 21 along the four radial lines indicated earlier in Fig. 8a. These support the conclusions taken from the contour plots - URANS shows closer agreement with the SDT data up to $r/R \approx 0.8$ in regards to the mean flow, while HRLES does slightly better near the casing - but it becomes evident that both methods struggle to predict the near-casing flow-field. As expected, HRLES predicts the local maxima in turbulent content in the blade wakes, with a deviation of $\pm 2 \, \text{m s}^{-1}$ from the experimental peak value.

The frequency content of the interstage velocity field was extracted from the time-dependent hot-wire measurements at station 1. The power spectral density (PSD) of this signal was then calculated for both the SDT data and the numerical results. Fourier transforms were smoothed using a Hann window with 50 % overlap and a bandwidth of 58.5 Hz. A few examples are presented in Fig. 24, for points labelled P_1, P_5 and P_6 according to Fig. 2b. Close to the hub (P_1), the BPF_1 and BPF_2 peaks of axial and radial velocities are predicted accurately in both URANS and HRLES. Higher frequencies see in general an underprediction of the tones, with exception of HRLES which overpredicts BPF_3 through BPF_6 axial velocity tone amplitudes. For the azimuthal velocity, URANS does a good job at predicting the tone levels up to BPF_2, while HRLES can only predict BPF_1 accurately. As expected, the URANS results are consistent with a signal mainly composed of BPF tones, lacking any broadband content. On the other hand, HRLES is able to capture the broadband content with good accuracy for the axial velocity component up to BPF_4, after which its levels start falling off of the hot-wire data. Azimuthal and radial velocity component broadband content is at least one order of magnitude lower in magnitude than the experimental data.

At location P_5, URANS does a good job at capturing the tonal content up to BPF3 for the axial velocity and BPF_4 for the remaining components. In regards to the HRLES results, an overprediction of the broadband levels is observed at frequencies below BPF_4, while the tones either fall short of (axial and radial components) or agree well with (azimuthal component) the hot-wire data on the same frequency range. PSD levels drop above BPF_4, although this brings them
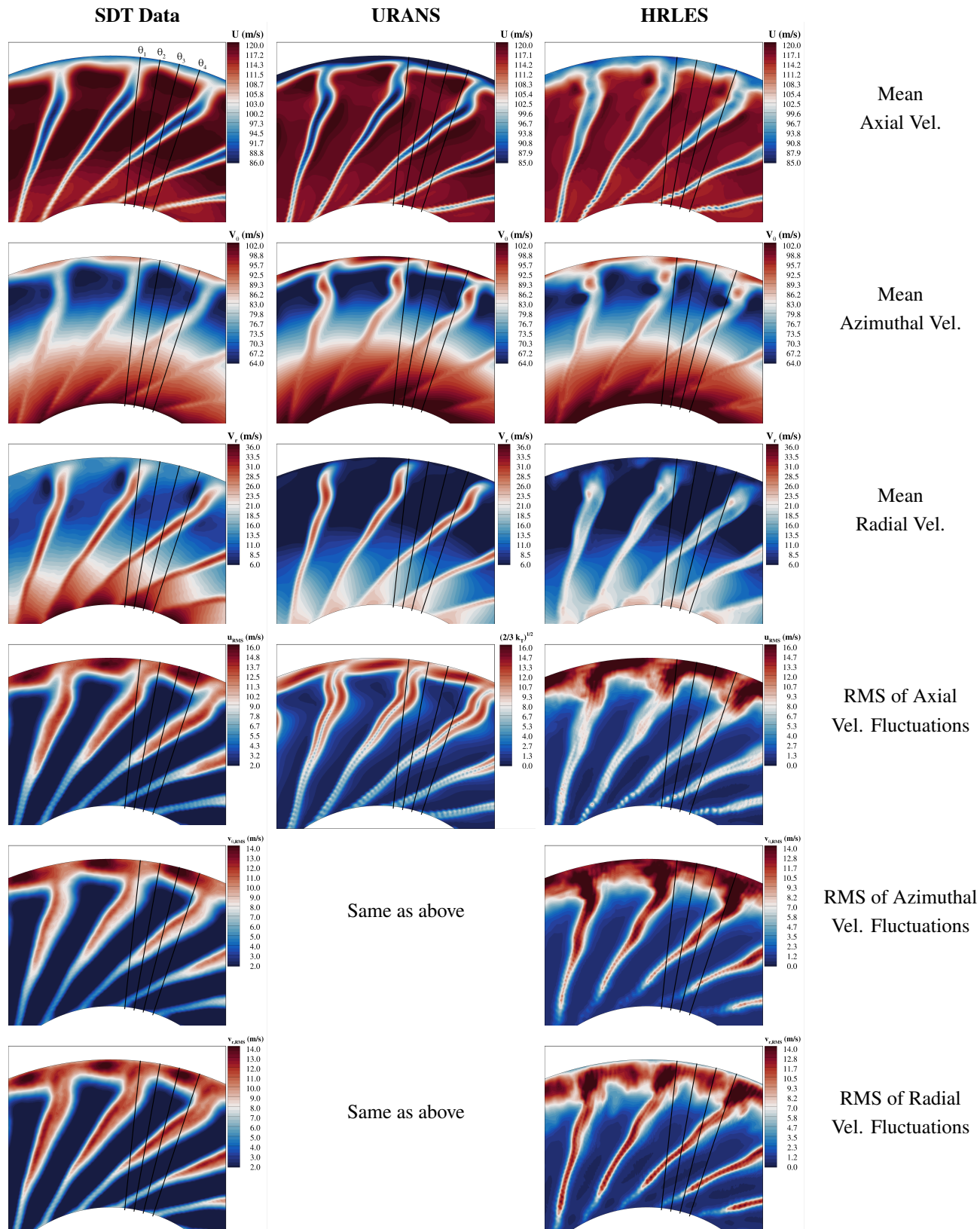
Fig. 21   Comparison of mean velocity and RMS velocity fluctuation components between SDT data (left column), URANS (center column) and HRLES (right column). Only axial component of RMS velocity fluctuations is shown for URANS since it was estimated from the TKE, as discussed in Sec. IV.A.3.
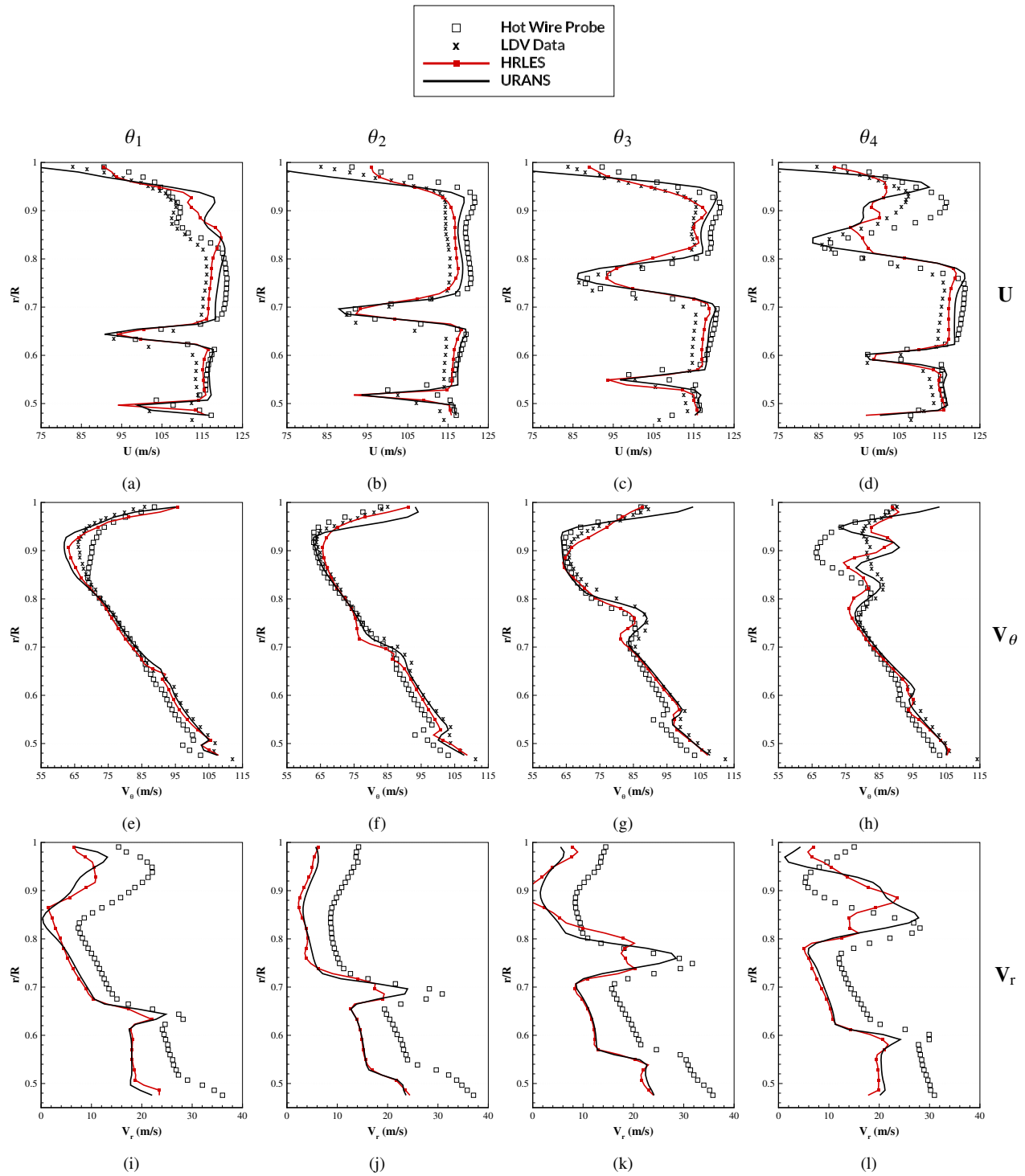
Fig. 22 Low-speed regime - mean axial, azimuthal and radial velocity profiles at hot-wire station 1. LDV data not available for radial velocity component V_r (bottom row).
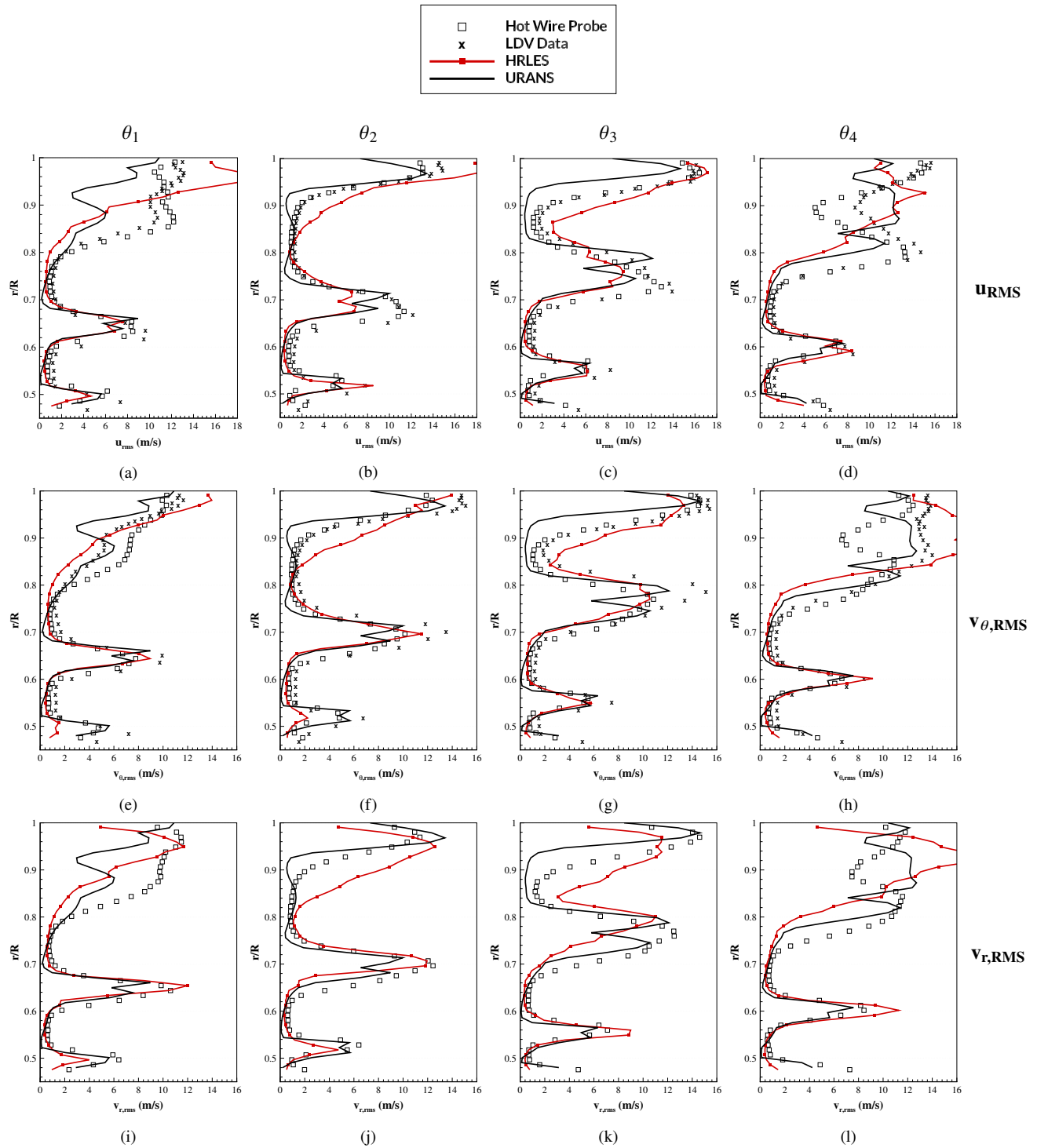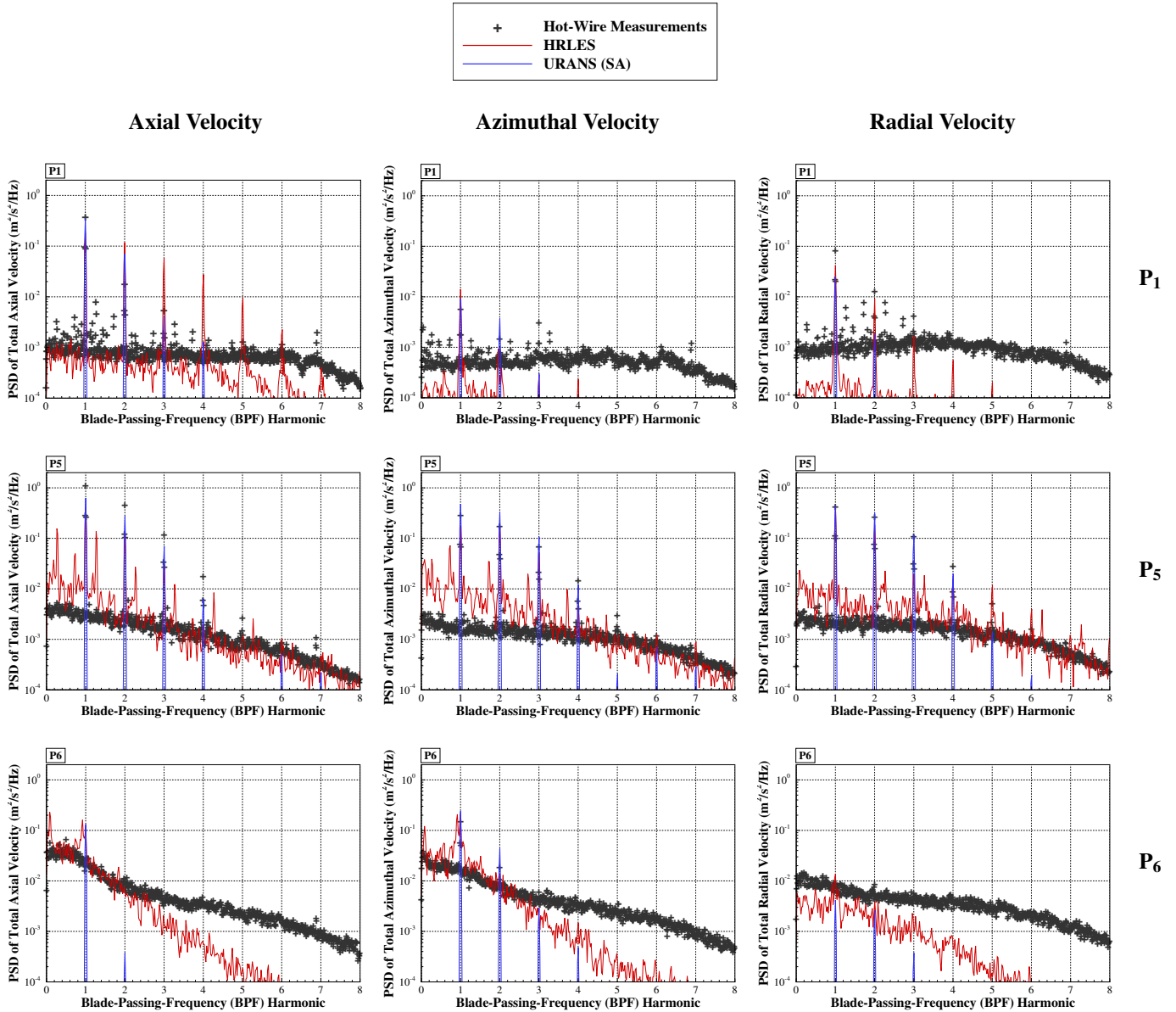
Fig. 23 Low-speed regime - RMS of axial, azimuthal and radial velocity fluctuations at hot-wire station 1. LDV data not available for radial velocity component V_r (bottom row).

Fig. 24 Frequency content of velocity data at several points at hot-wire station 1 for low-speed regime. From top to bottom rows the points move outwards in the radial direction, closer to the casing (see Fig. 2b). Comparison between SDT data (black), URANS (SA) results (blue) and HRLES results (red).

closer to the hot-wire measurements.

Finally, at location P_6 (very close to the casing), the tonal content of the signal is almost entirely obscured by the overwhelming broadband nature of the turbulent flow in this region. Due to this, URANS results underpredict the experimental PSD tone magnitudes at every BPF, except for BPF_1 which is the strongest at this location. A BPF_2 tone is also visible for the azimuthal velocity component, though it is overpredicted by URANS. The HRLES broadband content is in close agreement with the hot-wire data up to BPF_2 for the axial and azimuthal components, after which the grid no longer has sufficient spatial resolution. A similar trend is visible for the radial component, though the levels are underpredicted throughout the spectra.

C. Sideline/Take-Off (High-Speed) Condition

In this section, the high-speed take-off condition is analyzed. One of the key differences from the low-speed regime lies in the fan blade tip Mach number exceeding unity (M_{tip} = 1.085) at 12,657 RPM. Due to this, the acoustic behavior in the inlet changes and BPF tones become cut-on, meaning the rotor-locked tones are able to propagate upstream through the inlet of the fan. No hot-wire data is available from the SDT experiment at this condition in the interstage region.

The high-speed regime simulations ran using HRLES presented challenges that were not encountered on the low-speed condition. Firstly, the initialization procedure required modification due to robustness issues coming from the comparatively high fan rotational speed, which created supersonic flow regions around the blade stage sections during solution start-up that resulted in solution divergence if the initialization procedure outlined at the start of Sec. IV was followed. This behavior was only encountered when running the hybrid RANS/LES case, so the standard initialization procedure was followed for URANS. The HRLES simulation was then initialized with the solution obtained using URANS, and allowed to progress in time for several fan revolutions. However, a slope limiter was originally required when transitioning from the URANS solution to the HRLES simulation to prevent solution divergence (the Koren limiter was utilized). This simulation will be referred to as HRLES-L, as the limiter was turned on everywhere in the flow-field. Use of this limiter was later found to compromise the acoustic signal generated by the fan stage, as will be shown. Thus, a separate HRLES simulation was generated with the limiter turned off everywhere except for the rotor and OGV grids (HRLES-NL), where the problematic zones had been identified. This HRLES run used the already-established flow-field from the previous (slope-limited) simulation as the initial condition. No robustness issues were found with this setup, and the solution eventually reached statistical convergence.

The pressure field produced by the limiter-free HRLES simulation showed a much cleaner acoustic signal, without the spurious noise sources that were contaminating the HRLES-L solution. Surprisingly, however, the mean flow-field in the interstage was now compromised, and no longer showed the same rotational symmetry properties shared by the experimental data, the URANS flow solution and the previous HRLES-L simulation that employed a slope limiter. At the time of writing, this problem found on the high-speed condition is still under investigation. Nonetheless, representative results for both HRLES simulations will be presented in this section.

Another thing to note regarding the high-speed production simulations is that the 15 PPW acoustic constraint for BPF_2 would require almost double the number of grid points in each direction, resulting in an eight-fold increase in the total grid point count for the near-field. Thus, the same grid utilized for the low-speed case is used for the high-speed condition, since the computational cost of such simulation would not be justified by the scope of this work. This means that the BPF_2 tone is resolved using around 9 PPW at the high-speed condition, which may result in an inaccurate prediction of its sound pressure levels.

1. High-Speed Regime - Qualitative Comparison of CFD Modeling Approach

Figure 25 shows slices of the mean and instantaneous axial velocity across the stage in a similar layout to Fig. 16. Similar to the low-speed condition, both methods lie on top of the experimental data upstream of the fan stage. Downstream of the OGVs, the difference between URANS and HRLES is small, but HRLES captures the axial mean flow along the streamtrace shown in Fig. 25a with better agreement with the SDT data close to the fan stage. The axial velocity peak is overpredicted by URANS, but it decays at an increased rate compared to HRLES, which brings it closer to the experimental data past $x > 0.9$ m. The two HRLES solution profiles are similar, but the solution obtained when the limiter was off shows an improved behavior, recovering the URANS profile in the downstream section. Again, both URANS and HRLES agree well with the experiment in term of the radial and azimuthal velocity components. The instantaneous velocity contours and profiles shown on the right column show lobed patterns forming upstream of the fan blades and downstream of the OGVs. These are associated with the pressure waves forming in this high-speed condition, whose amplitude is large enough to visually impact the velocity field.

Figures 26 and 27 show slices of normalized vorticity magnitude at the high-speed regime. The same overall turbulent patterns observed at the low-speed regime are present, although the blade wakes are noticeably thinner at the high-speed condition. The HRLES solution shown corresponds to the simulation with no limiter, and it is representative of both HRLES runs considered. The vortex intensities in the high-speed condition are also at least twice as high (note the change in the color-scale compared to the low-speed case). URANS no longer predicts a steady vortex (in the rotating frame) downstream of the blade tip at the OGV trailing edge section (compare Figs. 18b and 27b). Instead, a thin trailing high-vorticity region is observed at each blade passage near the casing (Fig. 27a). Hybrid RANS/LES, on the other hand, shows an elliptical high-vorticity region downstream of the blade tip region, consistent with the presence
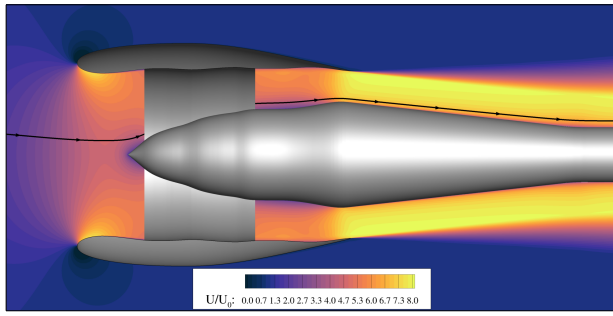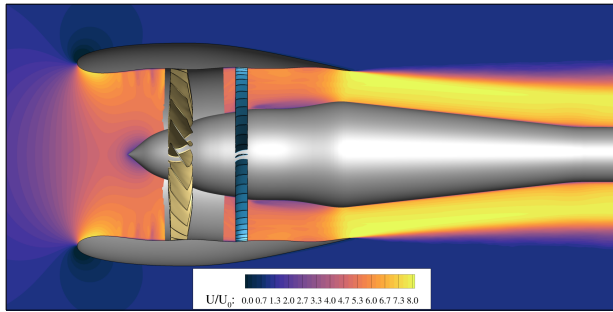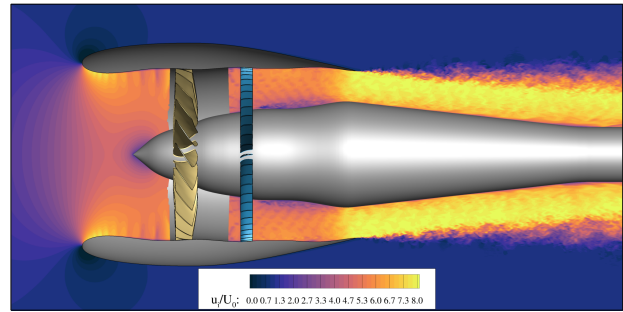
(a) SDT data, mean axial velocity.
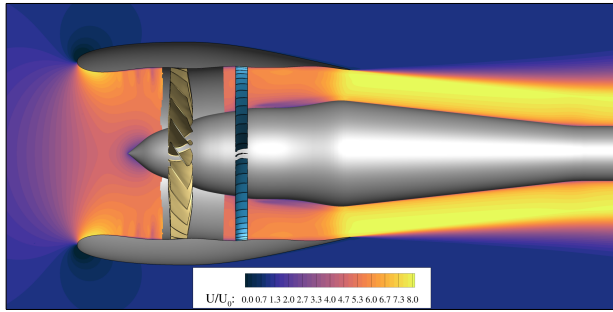
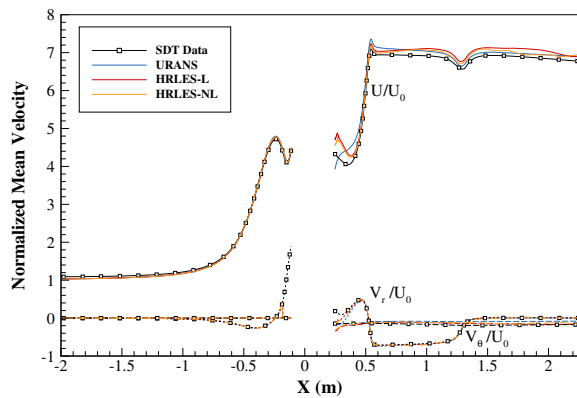(b) URANS (SA), mean axial velocity.
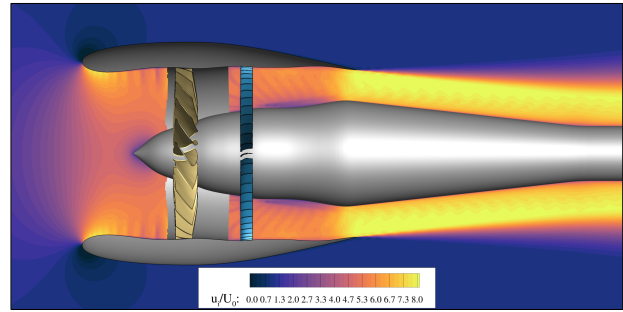
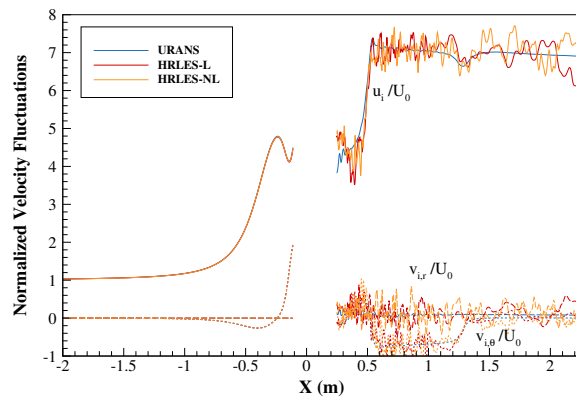(c) URANS (SA), instantaneous axial velocity.

(d) HRLES-NL, mean axial velocity.

(e) HRLES-NL, instantaneous axial velocity.

(f) Mean velocity profiles along streamtrace.

(g) Instantaneous velocity profiles along streamtrace.

Fig. 25   Slices of mean (left column) and instantaneous (right column) axial velocity from SDT data (top row) and both URANS and HRLES results (top center and top bottom rows, respectively) at the high-speed regime. Comparison of mean (left) and instantaneous (right) velocity profiles along the streamtrace illustrated in Fig. 16a (bottom row).

of a steady vortex in the rotating frame. Finally, the blade wakes remain coherent for a longer axial extent compared to the approach condition (see Figs. 17b and 26b).
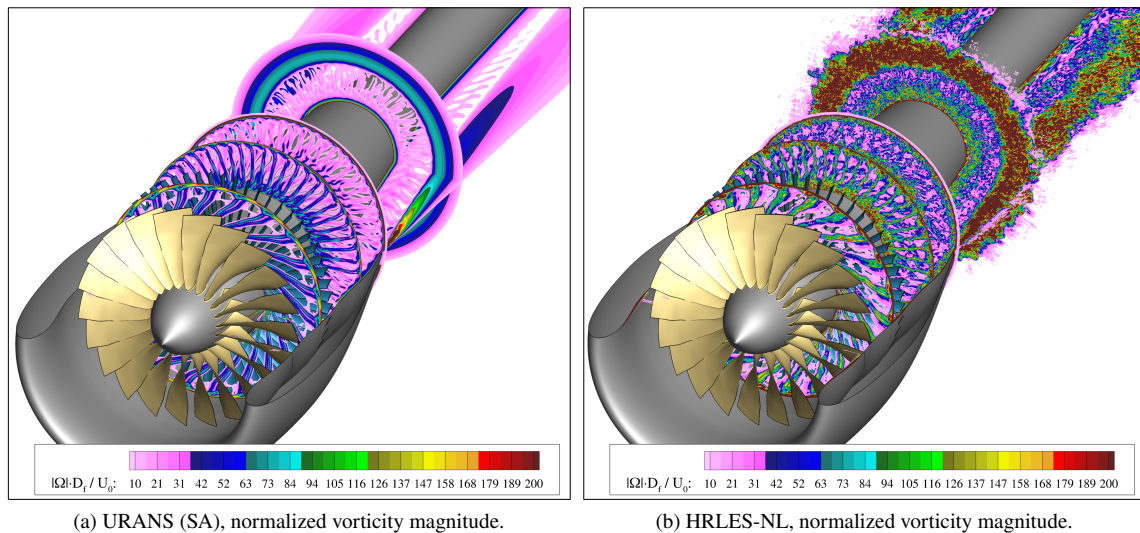

(a) URANS (SA), normalized vorticity magnitude.

(b) HRLES-NL, normalized vorticity magnitude.

Fig. 26 Snapshots of vorticity magnitude normalized by the fan diameter D_f and freestream velocity U_0 for URANS (left) and HRLES (right) at the high-speed regime. Values below 10 were hidden for clarity.

A snapshot of the pressure derivative field along a meridional plane is presented in Figs. 28a and 28c for URANS and both HRLES simulations considered. The issue discussed earlier regarding the HRLES simulation employing the Koren slope limiter (Fig. 28b) is now clearly visible: the fore-propagating tone originating from the inlet (present in the URANS solution) is entirely missing; so is the strong BPF_1 tone that is observed propagating downstream along the axial direction close to the hub wall in URANS; and the aft-propagating tones visible around the 110° to 170° sideline arc in the URANS solution are entirely disrupted by the spurious fluctuations originating from the exhaust. Comparison with the HRLES simulation ran without the limiter (Fig. reffig:high-speed-dp-dt-slice-overview-hrles) further emphasizes the numerical nature of the fluctuations present in the exhaust of the HRLES-L solution.

In contrast to what was observed at subsonic blade tip speeds (low-speed regime), rotor-locked tones are now visibly propagating upstream across the stage inlet in the URANS simulation. This is due to the BPF tones becoming cut-on at supersonic blade tip speeds, enabling upstream propagation through the inlet duct. Taking the limiter-free HRLES solution as reference, both URANS and hybrid RANS/LES predict the highest-amplitude pressure waves propagating at the 90° sideline angle in the exhaust, perpendicular to the axial direction. In addition, a fore-propagating tone originating from the exhaust is also similarly predicted by both models. The key differences between URANS and HRLES in the sound wave patterns forming around the fan stage are as follows. Firstly, the small-scale fluctuations originating from the nacelle trailing edge shear layer are only captured by HRLES. In addition, the BPF_2 tone propagating in the aft 160° to 180° arc is significantly stronger in the hybrid RANS/LES simulation. This tone is visible in the URANS figure, but dissipates rather quickly in comparison to HRLES. Finally, the fore-propagating BPF_1 tone in the inlet duct wraps around the nacelle leading edge, leading to tonal noise at sideline angles ranging from 45° to 135°. This is more apparent in the URANS simulation and may be related to an underprediction of the amplitude for this rotor-locked tone in the HRLES-NL solution.

It should be noted that the flow-field region where this BPF_2 tone is observed in the HRLES figure corresponds to the fine exhaust grid that obeys the 9 PPW acoustic constraint (15 PPW acoustic constraint in the low-speed regime), and that the FW-H surface that the near-field solution is interpolated onto sits inside this region. A noticeable difference in the resolution of the pressure field is observed in the coarse/fine grid interface along the conical region extending downstream from the nozzle exit, outside of which the BPF_2 tone is no longer captured. This highlights the importance of using sufficient PPW in the near-field to capture the highest frequencies of interest in the pressure field.

Axial slices of the pressure derivative field for the high-speed regime are presented in Fig. 29. Again, URANS shows the propagation of coherent spiral patterns correlated to the fan rotational speed. These are now also present at the fan stage inlet section, in contrast to the low-speed condition, for the reasons highlighted above. Compared to
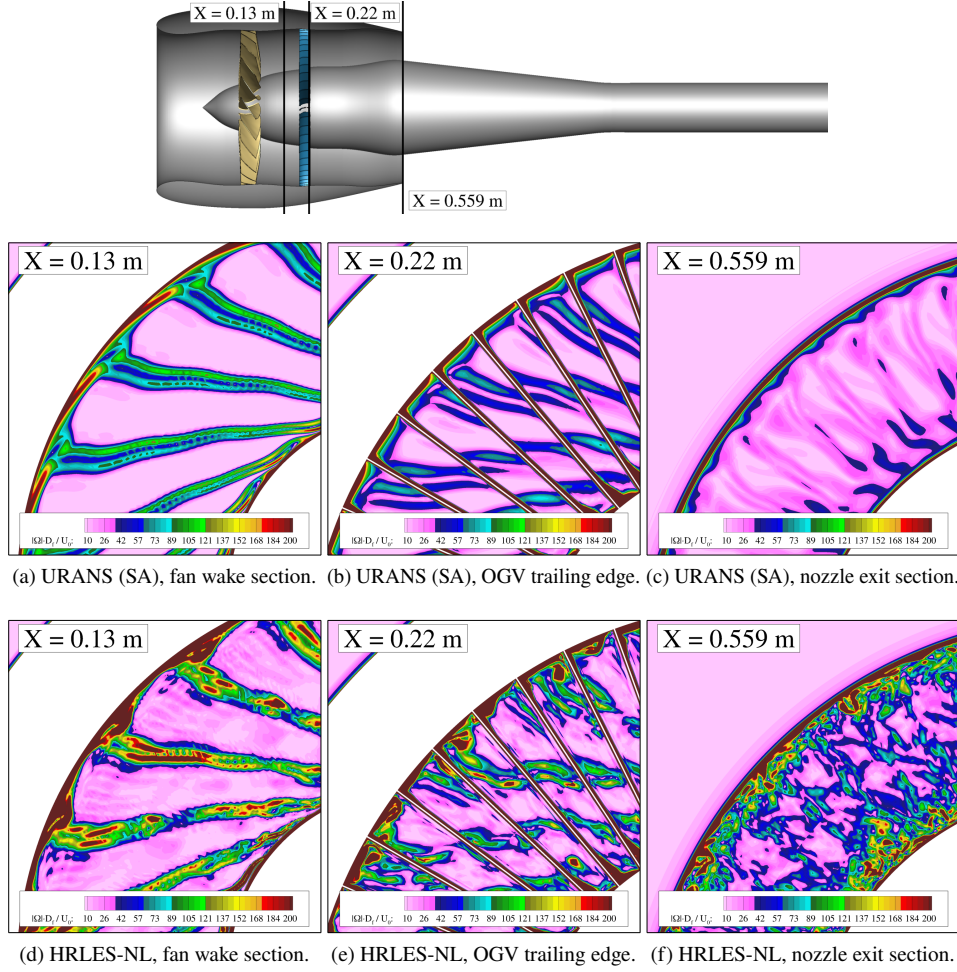
34

Fig. 27 **Snapshots of vorticity magnitude normalized by the fan diameter D_f and freestream velocity U_0 at several stations inside the fan stage for URANS (top row) and HRLES (bottom row) at the high-speed regime.**

URANS, hybrid RANS/LES shows similar sound wave patterns, especially in the first two slices, suggesting that the intensity of the tonal content along these slices is at least as high as the broadband noise. Also, note that the center slice taken at $x = 0.559$ m in Fig. 29 cuts through the highest-amplitude waves mentioned above, propagating at 90°, which explains why the tonal content looks mostly coherent. The same cannot be said regarding the slice taken further downstream at $x = 1.0$ m, where the fading spiral pattern observed in URANS is entirely disrupted by the broadband pressure fluctuations. Comparison of the slices taken for the two HRLES simulations shows the main differences occuring in the inlet duct and in the downstream exhaust region, where the simulation ran with the Koren limiter turned on shows the presence of spurious fluctuations that appear to be of numerical origin.

Finally, profiles of C_p and $C_{f,x}$ taken at several spanwise stations along the blade surface (those shown in Fig. 7) are included in Appendix D. Again, the main differences between URANS and HRLES occurs near the hub and blade tip regions. The differences observed between the two HRLES simulations do not explain the asymmetries mentioned above (discussed below).
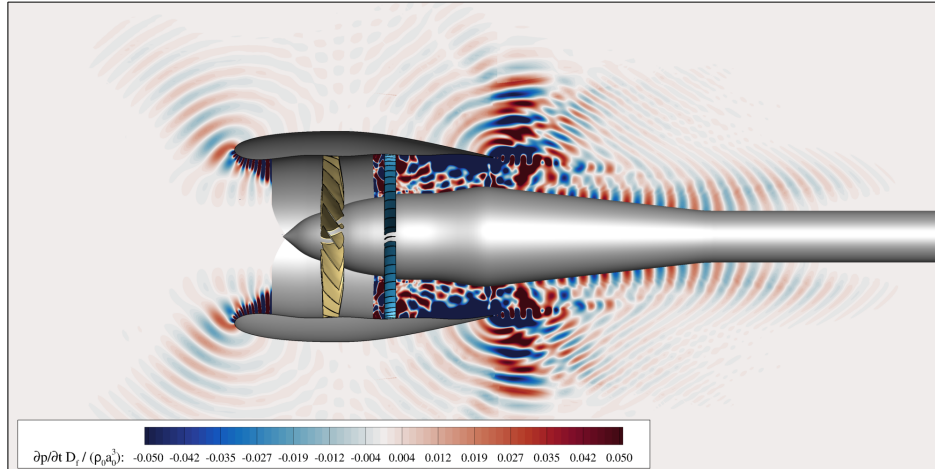
(a) URANS (SA), pressure waves pattern at a slice cutting through the fan stage.
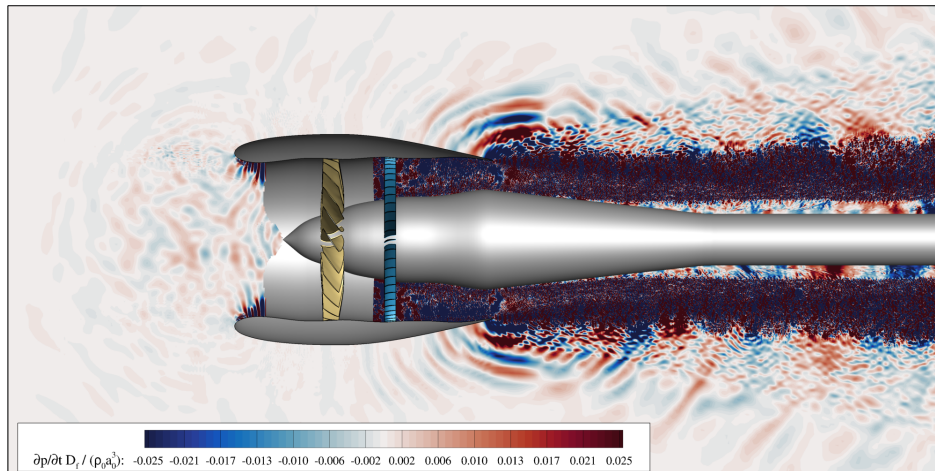
(b) HRLES-L, pressure waves pattern at a slice cutting through the fan stage.
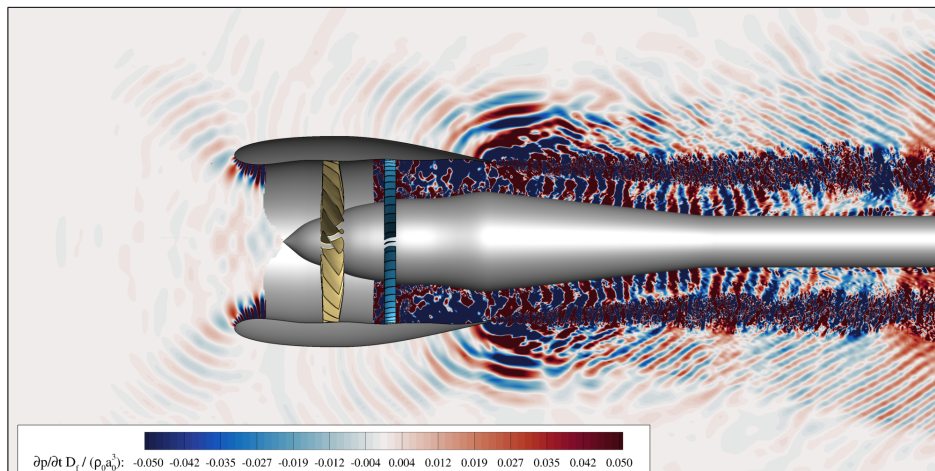
(c) HRLES-NL, pressure waves pattern at a slice cutting through the fan stage.

Fig. 28 Snapshots of pressure time derivative normalized by the fan diameter D_f, freestream density ρ_0 and sound speed a_0 for URANS (top) and HRLES (bottom) at the high-speed regime.

(a) URANS (SA), fan stage inlet section.

(b) URANS (SA), nozzle exit.

(c) URANS (SA), fan stage exhaust region.

(d) HRLES-L, fan stage inlet section.

(e) HRLES-L, nozzle exit.

(f) HRLES-L, fan stage exhaust region.

(g) HRLES-NL, fan stage inlet section.

(h) HRLES-NL, nozzle exit.

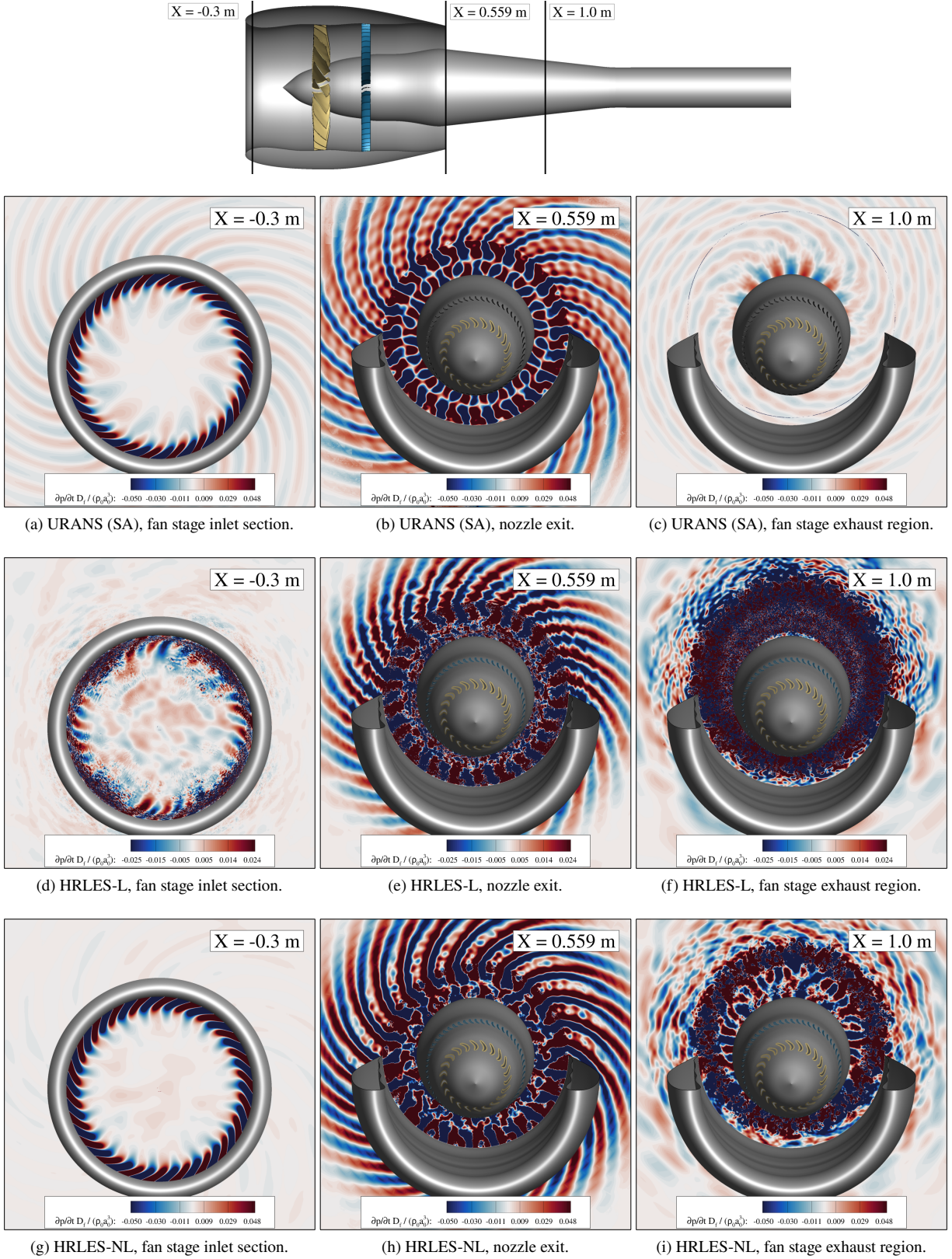(i) HRLES-NL, fan stage exhaust region.

Fig. 29 Snapshots of pressure time derivative normalized by the fan diameter D_f and freestream density ρ_0 and sound speed a_0 at several axial stations for URANS (top row) and HRLES (center row shows results with slope limiter, bottom row without) at the high-speed regime.

2. High-Speed Regime - Validation with SDT Data

Fan stage metrics predicted with URANS and hybrid RANS/LES are compared with the SDT data in Table 5. Excellent agreement is found on the total pressure and temperature ratios across the fan stage, with HRLES showing closer agreement with the experiment compared to URANS. Both models tend to slightly overpredict the mass flow rate. The maximum difference in this quantity is observed in the URANS solution, at just 1.79 % relative to the SDT data.

Table 5   Performance metrics results for the high-speed regime.

Case	Metric		
	Mass Flow Rate kg/s (% Δ) [†]	**Total Pressure Ratio (% Δ)**	**Total Temperature Ratio (% Δ)**
SDT Data [4]	43.998 (−)	1.490 (−)	1.137 (−)
URANS (SA)	44.787 (+1.79)	1.497 (+0.47)	1.136 (-0.09)
HRLES-L	44.523 (+1.19)	1.492 (+0.13)	1.135 (-0.18)
HRLES-NL	44.560 (+1.28)	1.493 (+0.20)	1.135 (-0.18)

Figure 30 shows the averaged velocity (top three rows) and RMS of velocity fluctuation (bottom three rows) components for the high-speed regime at hot-wire station 1. Radial velocity component data is not available from the SDT for this flow regime, since only the LDV data was collected at high-speed. Nonetheless, it is still shown for the numerical simulation cases. Comparing the two HRLES solutions sheds some light on the problem that was briefly mentioned in the introduction to this section. While the HRLES-L solution (which compromised the pressure field, and therefore the acoustic signal of the fan stage) maintains the rotational symmetry of each blade passage in a similar manner to the SDT data and the URANS results, the HRLES-NL solution shows asymmetries in the mean flow-field around each blade wake. This issue is currently under investigation, and will be subject to scrutiny prior to the characterization of the acoustic signature of the fan stage at high-speed. One of the potential causes for this behavior is the partial usage of the limiter in the rotor and OGV grids. To this end, a simulation employing no slope limiter would be desired and is running at the time of writing. Regardless of the limiter, both HRLES solutions predict stronger fluctuations in the half of the blade wake closest to the hub, in contrast to the SDT data, which shows larger unsteadiness in the outer half.

The two computational models are now compared and evaluated against the SDT data, taking the HRLES-L solution to represent the scale-resolved flow-field predicted by HRLES. The mean axial velocity predicted by URANS shows good agreement with the SDT data, especially near the casing. For both methods, the blade wake shape is mostly well-captured, except for the wake thickening that occurs in the outer half region. Near the hub, the numerically predicted wakes also present stronger twist compared to the experiment, which is made evident by noticing where the wake meets the hub boundary relative to the radial lines plotted in each contour. Another deficiency of the models is in the overprediction of the axial velocity deficit in the wakes. Correspondingly, both models overpredict the velocities in the regions downstream of the blade passages (red regions in the top row of Fig. 30). This is in agreement with the overpredicted mass flow rate discussed earlier. As for the mean azimuthal velocity, URANS seems to do a better job capturing the blade tip vortex and the blade wake thickness. Furthermore, URANS does not appear to suffer from the same large-scale unsteadiness observed predicted by hybrid RANS/LES in the half of the blade wake closest to the hub. Finally, velocity fluctuations in the blade wake and in the blade tip region are underpredicted by both methods.

Figures 31 and 32 highlight the deficiencies of each model discussed above in a quantitative manner, in terms of the mean and turbulent velocity fields, respectively, along the three radial lines plotted in Fig. 30. Overall, URANS predicts the mean flow-field with better accuracy compared to HRLES. The latter tends to over- and under-shoot the regions affected by the blade wakes. The HRLES-NL solution also shows oscillations of the mean velocity field around these regions. This is especially evident in the azimuthal velocity plots, which show a local minima-maxima-minima pattern in the fan blade wakes (see Fig. 31d). In regards to the turbulent velocity field, as discussed above, both models underpredict the amplitude of the velocity fluctuations in the blade wakes, and struggle to capture the near-casing flow-field downstream of the blade tip. In this region, the fluctuations extracted from the estimated TKE field in the URANS solution show trends that surprisingly match those of the SDT data, given how complex the blade tip flow-field
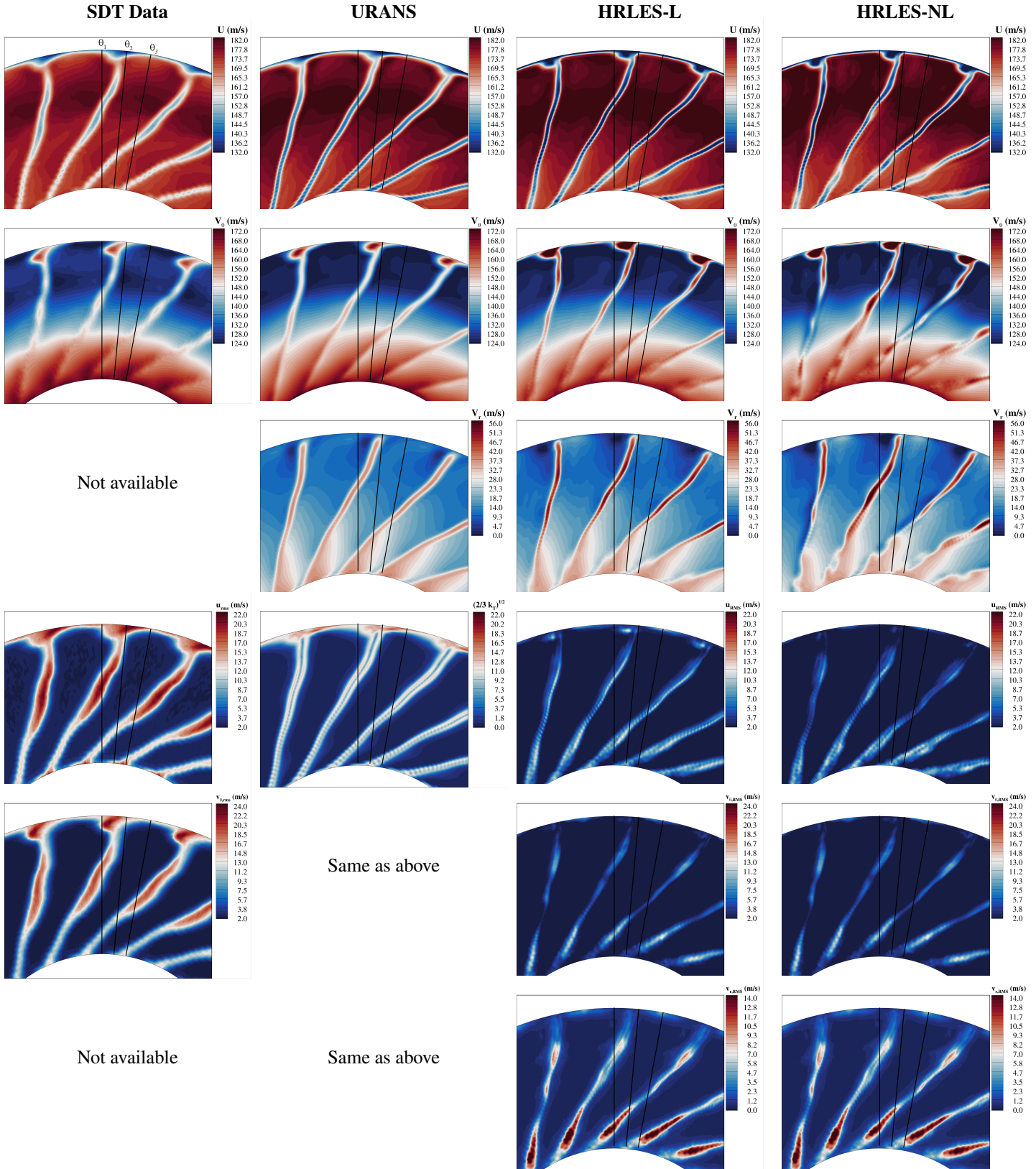
Fig. 30 Comparison of mean axial, azimuthal and radial velocity components (top three rows) and corresponding RMS velocity fluctuation components (bottom three rows) between SDT data (left column), URANS (center left column), HRLES using a Koren limiter (right center column) and HRLES with no limiter (right column).
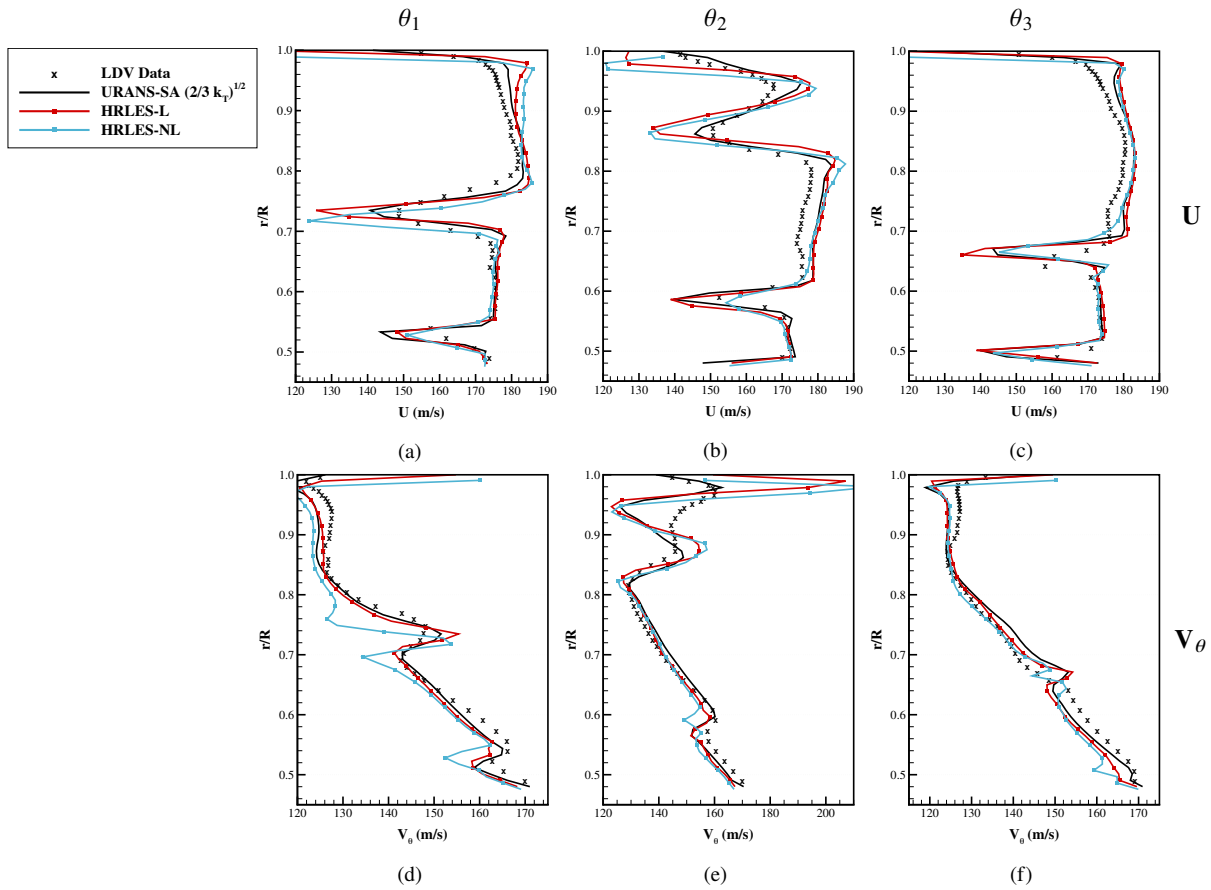
is upstream of this section.

Fig. 31 High-speed regime - mean axial and azimuthal velocity profiles at hot-wire station 1. Only LDV data is available for this condition.

Finally, Figure 33 shows contours of the relative Mach number in the vicinity of the fan blade tip at a constant-radius slice. The size and extent of the supersonic region in the pressure side of the blades agrees well with the experimental LDV data for both URANS and HRLES, although the relative Mach number inside this region appears to be slightly overpredicted in both cases. The opposite is true in the suction side of the blade, where the SDT data shows a higher relative Mach number near the mid-chord section compared to the numerical results.
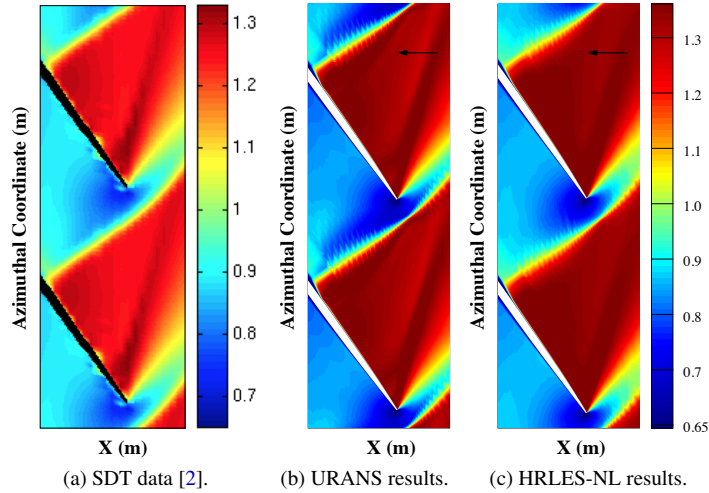
Fig. 32 High-speed regime - axial and azimuthal velocity fluctuations at hot-wire station 1. Only LDV data is available for this condition.

Fig. 33 Contours of relative Mach number near the blade tip (r = 0.2631 m). SDT data (left), URANS (center) and HRLES (right) results. Flow direction is right to left.

V. Computational Cost

Computational cost requirements for the four production runs produced in this work using URANS and hybrid RANS/LES are compared in Table 6. As mentioned previously, the grid system used for the HRLES had to be modified such that no overset was present in the exhaust region in the radial direction. This resulted in an increase in the number of points for the HRLES grid system, since a single grid block obeying the 15 points-per-wavelength requirement for BPF_2 had to be used. This constraint was still obeyed in the URANS grid system, but the ability to have overset in the radial direction meant that several grid blocks could be overset with an increasing number of grid points in the azimuthal direction with increasing radius. This resulted in a grid system with about 20 % more points for the HRLES simulations.

This difference alone only partly explains the 3× increased cost of HRLES compared to URANS. The main driving factor for the increased cost in HRLES is the number of sub-iterations required in pseudo-time to achieve a level of flow and turbulence residual reduction per time-step that was deemed sufficient. While both residuals dropped 4 orders of magnitude with just 3 sub-iterations in URANS, those in the hybrid RANS/LES simulations plateaued after 5-6 sub-iterations, almost reaching 4 orders of magnitude reductions. Nevertheless, to ensure each time-step was fully converged, a fixed number of 12 sub-iterations per time-step was used in the HRLES simulations. This resulted in a significantly longer core-time per fan revolution for this model, as can be seen in Table 6.

VI. Conclusions and Future Work

The extensive experimental dataset collected in the NASA SDT campaign was utilized in this work to validate a sliding mesh implementation in the LAVA solver framework on a complex rotating fan rig configuration. Conditions representative of take-off and approach were simulated using both URANS and HRLES approaches. This work is the first part of a two-part study, and focuses on both the aerodynamic and turbulent characterization of the flow-field. The second part of the study, concerning the accurate prediction of the acoustic signature of the fan rig, will be published at a later date.

Sensitivity to grid refinement, time-step size and turbulence model closure utilized within a subset of the SA variants available in the LAVA solver have been assessed. Grid refinement and time-step size sensitivity was found to be small in terms of quantified aerodynamic and turbulent quantities. Both parameters were constrained by acoustic requirements established for the numerical scheme utilized in the production runs. The baseline SA turbulence model was observed to provide an instantaneous flow-field closest to that obtained via hot-wire measurements in the interstage region, free of the vortical structures that compromised the acoustic signature of the fan stage.

Overall, the results support the use of the newly-implemented sliding mesh technique to simulate turbomachinery components in relative rotating motion. The aerodynamic and turbulent characterization of the flow-field in the interstage

Table 6   Computational cost summary for the production runs performed in this work.

| | Production Run | | | |
| | URANS | | HRLES | |
Attribute	Low-speed	High-speed	Low-speed	High-speed
Solution points	385M		469M	
Time-step size (µs)	3.56	2.20	3.56	2.20
Nodes used for simulation	214 Broadwell (28 cores/node)		180 SkyLake (40 cores/node)	200 SkyLake (40 cores/node)
Core-time per compute point per time-step (µs)	105.1	83.9	246.4	265.9
Core-time for flow initialization	197,000 hours	243,000 hours	465,000 hours	455,000 hours
Core-time per fan revolution	24,250 hours	19,300 hours	68,400 hours	73,800 hours
Total core-time needed for 10 fan revolutions	242,500 hours	193,500 hours	684,000 hours	738,000 hours
Total NAS SBUs [†]	15,600	15,500	45,700	45,900

[†] NASA Advanced Supercomputing Standard Billing Unit, calculated as described in [37].

region showed good agreement with the SDT data, laying the groundwork for the second part of the study focusing on the acoustics of the fan rig. The far-field noise signature will be compared with the SDT data in a future publication, using the Ffowcs Williams and Hawkings (FW-H) permeable surface method to propagate the near-field pressure signal to the far-field sideline microphone array. The close agreement between URANS and hybrid RANS/LES in these metrics supports the use of standard URANS for these types of configurations if broadband noise can be ignored, given its lower cost and improved sub-iteration convergence behavior.

Low-speed results representative of approach conditions show stage performance metrics in excellent agreement with the SDT data for both URANS and HRLES. Mean velocity components agree well with the hot-wire station 1 data for both methods, except for the radial velocity component which presents a constant shift from the SDT data, underpredicting it by about $6\,\mathrm{m\,s^{-1}}$ to $10\,\mathrm{m\,s^{-1}}$. Hybrid RANS/LES outperforms URANS when it comes to the velocity fluctuations at the same location up to a radial distance of about 80 % of the casing radius. Past this radial location, where blade tip vortices that have been convected downstream are present, both methods struggle to accurately predict the turbulent flow, but HRLES overpredicts these fluctuations more so than those extracted from the estimated TKE in URANS. This is not surprising given that the complex flow in this region originates from the small blade tip gap of approximately 0.5 mm, and is thus contained in a region that is treated in URANS mode. The acoustic signature of the two methods is very distinct, mainly due to the inability for URANS to capture broadband noise. This is evident in the lack of fore-propagating inlet noise that URANS predicts, and in the small-scale fluctuations following the shear layer that only HRLES is able to resolve.

Finally, a high-speed condition representative of take-off was also simulated using both models. Both models showed fan stage performance metrics with less than 2 % agreement with the SDT data. While URANS showed similar convergence behavior as in the low-speed case, HRLES presented challenges that were unique to this regime. One of those challenges is related to the supersonic blade tip speed characterizing this condition. The unsteady flow-field would fail to converge unless a slope limiter was used when initializing the flow-field using the high-speed URANS solution. Use of this limiter generated spurious numerical fluctuations that contaminated the acoustic signal. A limiter-free HRLES solution was eventually obtained, characterized by a much cleaner acoustic field, but compromising the quality

of the flow-field in the interstage region. This issue is currently under investigation, and will be subject of further scrutiny prior to characterizing the acoustic signature of the fan stage in Part II of this study. The challenges encountered with HRLES may be the reason why the URANS interstage flow-field shows better agreement with the experimental data. Nonetheless, both models struggle to accurately predict the thickness of the blade wake, as well as the near-casing flow-field downstream of the blade tip.

VII. Acknowledgments

References

[1] Envia, E., "Fan Noise Reduction: An Overview," *International Journal of Aeroacoustics*, Vol. 1, No. 1, 2002, pp. 43–64. https://doi.org/10.1260/1475472021502668, URL https://doi.org/10.1260/1475472021502668.

[2] Podboy, G., Krupar, M., Helland, S., and Hughes, C., "Steady and unsteady flow field measurements within a NASA 22 inch fan model," *40th AIAA Aerospace Sciences Meeting & Exhibit*, Reno, NV, 2002. https://doi.org/10.2514/6.2002-1033, URL https://arc.aiaa.org/doi/abs/10.2514/6.2002-1033.

[3] Hughes, C., Jeracki, R., Woodward, R., and Miller, C., "Fan Noise Source Diagnostic Test - Rotor Alone Aerodynamic Performance Results," *8th AIAA/CEAS Aeroacoustics Conference & Exhibit*, Breckenridge, CO, 2002. https://doi.org/10.2514/6.2002-2426, URL https://arc.aiaa.org/doi/abs/10.2514/6.2002-2426.

[4] Hughes, C., "Aerodynamic performance of scale-model turbofan outlet guide vanes designed for low noise," *40th AIAA Aerospace Sciences Meeting & Exhibit*, Reno, NV, 2002. https://doi.org/10.2514/6.2002-374, URL https://arc.aiaa.org/doi/abs/10.2514/6.2002-374.

[5] Heidelberg, L., "Fan Noise Source Diagnostic Test - Tone Modal Structure Results," *8th AIAA/CEAS Aeroacoustics Conference & Exhibit*, Breckenridge, CO, 2002. https://doi.org/10.2514/6.2002-2428, URL https://arc.aiaa.org/doi/abs/10.2514/6.2002-2428.

[6] Premo, J., and Joppa, P., "Fan Noise Source Diagnostic Test - Wall Measured Circumferential Array Mode Results," *8th AIAA/CEAS Aeroacoustics Conference & Exhibit*, Breckenridge, CO, 2002. https://doi.org/10.2514/6.2002-2429, URL https://arc.aiaa.org/doi/abs/10.2514/6.2002-2429.

[7] Woodward, R., Hughes, C., Jeracki, R., and Miller, C., "Fan Noise Source Diagnostic Test – Far-field Acoustic Results," *8th AIAA/CEAS Aeroacoustics Conference & Exhibit*, Breckenridge, CO, 2002. https://doi.org/10.2514/6.2002-2427, URL https://arc.aiaa.org/doi/abs/10.2514/6.2002-2427.

[8] Envia, E., "Fan Noise Source Diagnostics Test - Vane Unsteady Pressure Results," *8th AIAA/CEAS Aeroacoustics Conference & Exhibit*, Breckenridge, CO, 2002. https://doi.org/10.2514/6.2002-2430, URL https://arc.aiaa.org/doi/abs/10.2514/6.2002-2430.

[9] Podboy, G., Krupar, M., Hughes, C., and Woodward, R., "Fan Noise Source Diagnostic Test- LDV Measured Flow Field Results," *8th AIAA/CEAS Aeroacoustics Conference & Exhibit*, Breckenridge, CO, 2002. https://doi.org/10.2514/6.2002-2431, URL https://arc.aiaa.org/doi/abs/10.2514/6.2002-2431.

[10] Kiris, C. C., Housman, J. A., Barad, M. F., Brehm, C., Sozer, E., and Moini-Yekta, S., "Computational framework for Launch, Ascent, and Vehicle Aerodynamics (LAVA)," *Aerospace Science and Technology*, Vol. 55, 2016, pp. 189–219. https://doi.org/10.1016/j.ast.2016.05.008, URL https://www.sciencedirect.com/science/article/pii/S127096381630178X.

[11] Hah, C., and Romeo, M., "LES Investigation of Wake Development in a Transonic Fan Stage for Aeroacoustic Analysis," *23rd International Symposium on Air Breathing Engines*, Manchester, United Kingdom, 2017. URL https://ntrs.nasa.gov/api/citations/20170008798/downloads/20170008798.pdf.

[12] Moreau, S., "Turbomachinery Noise Predictions: Present and Future," *Acoustics*, Vol. 1, 2019, pp. 92–116. https://doi.org/10.3390/acoustics1010008.

[13] Casalino, D., Hazir, A., and Mann, A., "Turbofan Broadband Noise Prediction Using the Lattice Boltzmann Method," *AIAA Journal*, Vol. 56, No. 2, 2018, pp. 609–628. https://doi.org/10.2514/1.J055674, URL https://doi.org/10.2514/1.J055674.

[14] Gonzalez-Martino, I., and Casalino, D., "Fan Tonal and Broadband Noise Simulations at Transonic Operating Conditions Using Lattice-Boltzmann Methods," *2018 AIAA/CEAS Aeroacoustics Conference*, Atlanta, GA, 2018. https://doi.org/10.2514/6.2018-3919, URL https://arc.aiaa.org/doi/abs/10.2514/6.2018-3919.

[15] Shur, M., Strelets, M., Travin, A., Spalart, P., and Suzuki, T., "Unsteady Simulations of a Fan/Outlet-Guide-Vane System: Aerodynamics and Turbulence," *AIAA Journal*, Vol. 56, No. 6, 2018, pp. 2283–2297. https://doi.org/10.2514/1.J056645, URL https://doi.org/10.2514/1.J056645.

[16] Suzuki, T., Spalart, P. R., Shur, M. L., Strelets, M. K., and Travin, A. K., "Unsteady Simulations of a Fan/Outlet-Guide-Vane System: Tone–Noise Computation," *AIAA Journal*, Vol. 56, No. 9, 2018, pp. 3558–3569. https://doi.org/10.2514/1.J056646, URL https://doi.org/10.2514/1.J056646.

[17] Suzuki, T., Spalart, P. R., Shur, M. L., Strelets, M. K., and Travin, A. K., "Unsteady Simulations of a Fan/Outlet-Guide-Vane System: Broadband-Noise Computation," *AIAA Journal*, Vol. 57, No. 12, 2019, pp. 5168–5181. https://doi.org/10.2514/1.J058177, URL https://doi.org/10.2514/1.J058177.

[18] Deck, S., and Renard, N., "Towards an enhanced protection of attached boundary layers in hybrid RANS/LES methods," *Journal of Computational Physics*, Vol. 400, 2020, p. 108970. https://doi.org/10.1016/j.jcp.2019.108970, URL https://www.sciencedirect.com/science/article/pii/S0021999119306758.

[19] Spalart, P., and Allmaras, S., "A one-equation turbulence model for aerodynamic flows," *30th Aerospace Sciences Meeting & Exhibit*, Reno, NV, 1992. https://doi.org/10.2514/6.1992-439, URL https://arc.aiaa.org/doi/abs/10.2514/6.1992-439.

[20] Shur, M. L., Strelets, M. K., Travin, A. K., and Spalart, P. R., "Turbulence Modeling in Rotating and Curved Channels: Assessing the Spalart-Shur Correction," *AIAA Journal*, Vol. 38, No. 5, 2000, pp. 784–792. https://doi.org/10.2514/2.1058, URL https://doi.org/10.2514/2.1058.

[21] Spalart, P., "Strategies for turbulence modelling and simulations," *International Journal of Heat and Fluid Flow*, Vol. 21, No. 3, 2000, pp. 252–263. https://doi.org/10.1016/S0142-727X(00)00007-2, URL https://www.sciencedirect.com/science/article/pii/S0142727X00000072.

[22] Spalart, P., "Trends in turbulence treatments," *Fluids 2000 Conference & Exhibit*, Denver, CO, 2000. https://doi.org/10.2514/6.2000-2306, URL https://arc.aiaa.org/doi/abs/10.2514/6.2000-2306.

[23] Spalart, P. R., Deck, S., Shur, M. L., Squires, K. D., Strelets, M. K., and Travin, A., "A New Version of Detached-eddy Simulation, Resistant to Ambiguous Grid Densities," *Theoretical and Computational Fluid Dynamics*, Vol. 20, No. 3, 2006, p. 181. https://doi.org/10.1007/s00162-006-0015-0, URL https://doi.org/10.1007/s00162-006-0015-0.

[24] Deck, S., "Recent improvements in the Zonal Detached Eddy Simulation (ZDES) formulation," *Theoretical and Computational Fluid Dynamics*, Vol. 26, No. 6, 2012, pp. 523–550. https://doi.org/10.1007/s00162-011-0240-z, URL https://doi.org/10.1007/s00162-011-0240-z.

[25] Caruelle, B., and Ducros, F., "Detached-Eddy Simulations of Attached and Detached Boundary Layers," *International Journal of Computational Fluid Dynamics*, Vol. 17, 2003. https://doi.org/10.1080/10618560310001598880, URL https://www.researchgate.net/publication/228775143_Detached-Eddy_Simulations_of_Attached_and_Detached_Boundary_Layers.

[26] Ghate, A. S., Kenway, G. K., Stich, G.-D., Browne, O. M., Housman, J. A., and Kiris, C. C., "Transonic lift and drag predictions using Wall-Modelled Large Eddy Simulations," *AIAA Scitech 2021 Forum*, 2021. https://doi.org/10.2514/6.2021-1439, URL https://arc.aiaa.org/doi/abs/10.2514/6.2021-1439.

[27] Housman, J. A., Stich, G.-D., Kocheemoolayil, J. G., and Kiris, C. C., "Predictions of Slat Noise from the 30P30N at High Angles of Attack using Zonal Hybrid RANS-LES," *25th AIAA/CEAS Aeroacoustics Conference*, Delft, The Netherlands, 2019. https://doi.org/10.2514/6.2019-2438, URL https://arc.aiaa.org/doi/abs/10.2514/6.2019-2438.

[28] Stich, D., Housman, J. A., Kocheemoolayil, J. G., Barad, M. F., Cadieux, F., and Kiris, C. C., "Application of Lattice Boltzmann and Navier-Stokes Methods to NASA's Wall Mounted Hump," *2018 Fluid Dynamics Conference*, Atlanta, GA, 2018. https://doi.org/10.2514/6.2018-3855, URL https://arc.aiaa.org/doi/abs/10.2514/6.2018-3855.

[29] Browne, O. M., Housman, J. A., Kenway, G. K., Ghate, A. S., and Kiris, C. C., "A Hybrid RANS-LES Perspective for the High Lift Common Research Model Using LAVA," *AIAA Aviation 2022 Forum*, Chicago, IL, 2022. https://doi.org/10.2514/6.2022-3523, URL https://arc.aiaa.org/doi/abs/10.2514/6.2022-3523.

[30] Vinokur, M., "Conservation equations of gasdynamics in curvilinear coordinate systems," *Journal of Computational Physics*, Vol. 14, No. 2, 1974, pp. 105–125. https://doi.org/10.1016/0021-9991(74)90008-4, URL https://www.sciencedirect.com/science/article/pii/0021999174900084.

[31] Housman, J. A., and Kiris, C. C., "Structured Overlapping Grid Simulations of Contra-Rotating Open Rotor Noise," *54th AIAA Aerospace Sciences Meeting*, San Diego, CA, 2016. https://doi.org/10.2514/6.2016-0814, URL https://arc.aiaa.org/doi/abs/10.2514/6.2016-0814.

[32] Housman, J. A., and Kiris, C. C., "Slat Noise Predictions using Higher-Order Finite-Difference Methods on Overset Grids," *22nd AIAA/CEAS Aeroacoustics Conference*, Lyon, France, 2016. https://doi.org/10.2514/6.2016-2963, URL https://arc.aiaa.org/doi/abs/10.2514/6.2016-2963.

[33] Steger, J. L., and Benek, J. A., "On the use of composite grid schemes in computational aerodynamics," *Computer Methods in Applied Mechanics and Engineering*, Vol. 64, No. 1, 1987, pp. 301–320. https://doi.org/10.1016/0045-7825(87)90045-4, URL https://www.sciencedirect.com/science/article/pii/0045782587900454.

[34] Kenway, G. K., Mishra, A., Secco, N. R., Duraisamy, K., and Martins, J. R. R. A., "An Efficient Parallel Overset Method for Aerodynamic Shape Optimization," *58th AIAA/ASCE/AHS/ASC Structures, Structural Dynamics, and Materials Conference*, Grapevine, TX, 2017. https://doi.org/10.2514/6.2017-0357, URL https://arc.aiaa.org/doi/abs/10.2514/6.2017-0357.

[35] Zhang, X., Ni, S., and He, G., "A pressure-correction method and its applications on an unstructured Chimera grid," *Computers & Fluids*, Vol. 37, 2008, pp. 993–1010. https://doi.org/10.1016/j.compfluid.2007.07.019, URL https://doi.org/10.1016/j.compfluid.2007.07.019.

[36] Zhang, B., and Liang, C., "A simple, efficient, and high-order accurate curved sliding-mesh interface approach to spectral difference method on coupled rotating and stationary domains," *Journal of Computational Physics*, Vol. 295, 2015, pp. 147–160. https://doi.org/10.1016/j.jcp.2015.04.006, URL https://www.sciencedirect.com/science/article/pii/S0021999115002466.

[37] "NASA High-End Computing: Standard Billing Units," , 2022. URL https://hec.nasa.gov/user/policies/sbus.html.

A. Grid Refinement Study C_p and $C_{f,x}$ Blade Surface Profiles

(a) C_p, Z = 0.11 m.　　(b) C_p, Z = 0.15 m.　　(c) C_p, Z = 0.20 m.　　(d) C_p, Z = 0.25 m.　　(e) C_p, Z = 0.272 m.

(f) $C_{f,x}$, Z = 0.11 m.　　(g) $C_{f,x}$, Z = 0.15 m.　　(h) $C_{f,x}$, Z = 0.20 m.　　(i) $C_{f,x}$, Z = 0.25 m.　　(j) $C_{f,x}$, Z = 0.272 m.
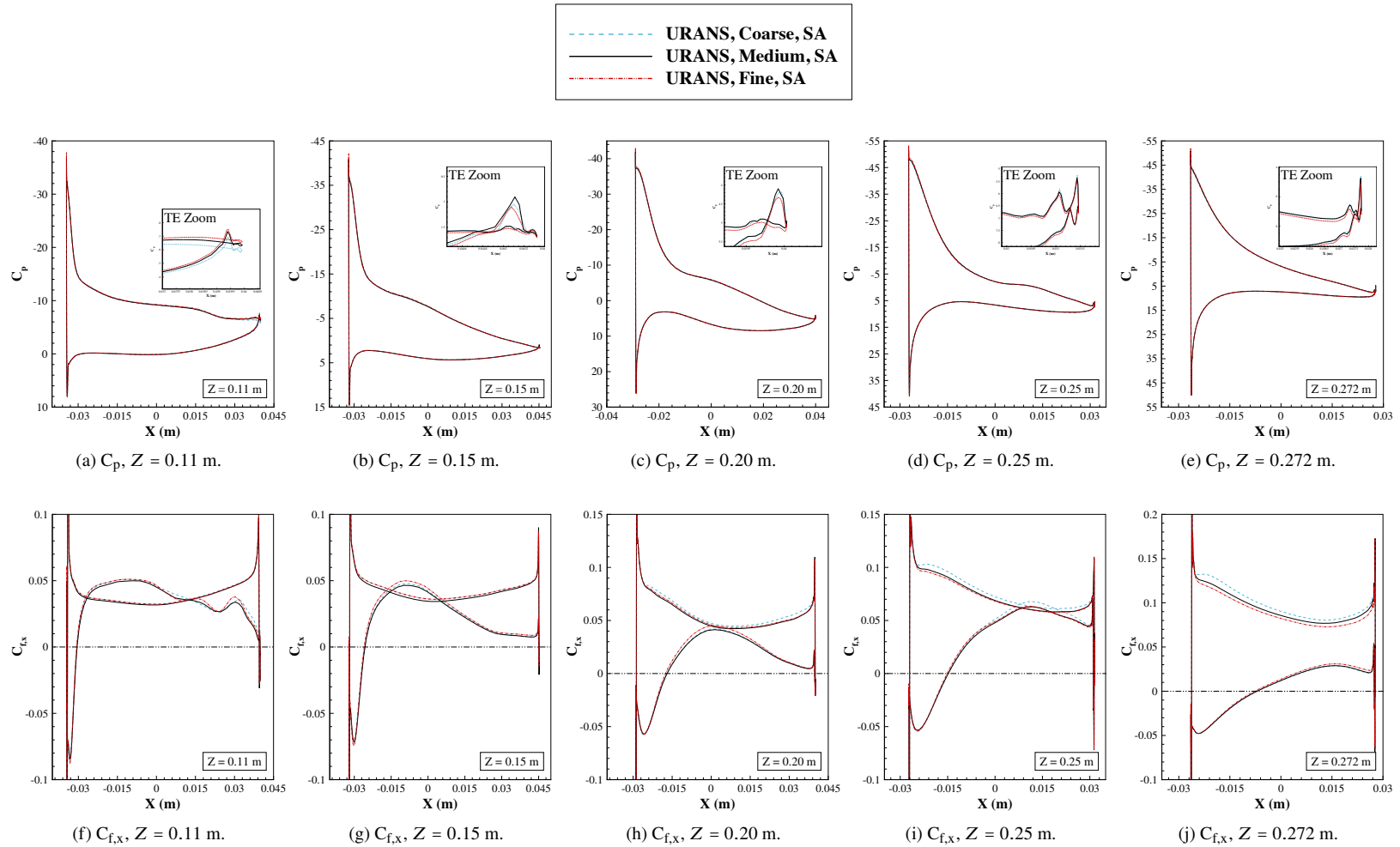
Fig. A.1   Comparison of pressure coefficient (C_p) and axial skin friction coefficient ($C_{f,x}$) surface profiles taken at different spanwise sections along the blade for the three grid refinement levels run using URANS on the low-speed regime. Solution data taken from averaged flow-field.

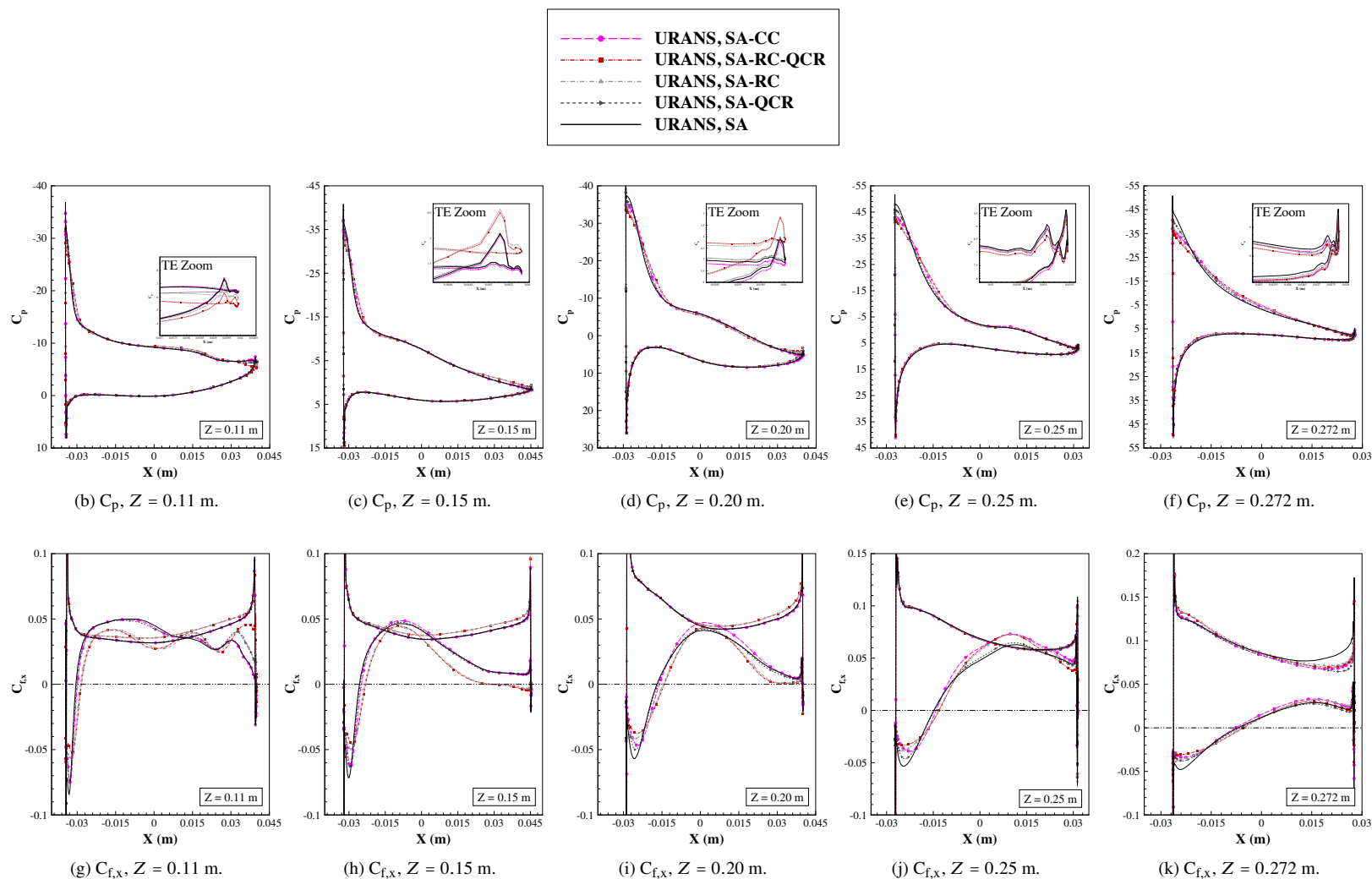## B. Turbulence Model Sensitivity C_p and $C_{f,x}$ Blade Surface Profiles

Fig. B.1 **Comparison of pressure coefficient (C_p) and axial skin friction coefficient ($C_{f,x}$) surface profiles taken at different spanwise sections along the blade for the different turbulence models run using URANS on the low-speed regime. Solution data taken from averaged flow-field.**

C. Low-Speed Regime C_p and $C_{f,x}$ Blade Surface Profiles

(b) C_p, Z = 0.11 m. (c) C_p, Z = 0.15 m. (d) C_p, Z = 0.20 m. (e) C_p, Z = 0.25 m. (f) C_p, Z = 0.272 m.

(g) $C_{f,x}$, Z = 0.11 m. (h) $C_{f,x}$, Z = 0.15 m. (i) $C_{f,x}$, Z = 0.20 m. (j) $C_{f,x}$, Z = 0.25 m. (k) $C_{f,x}$, Z = 0.272 m.
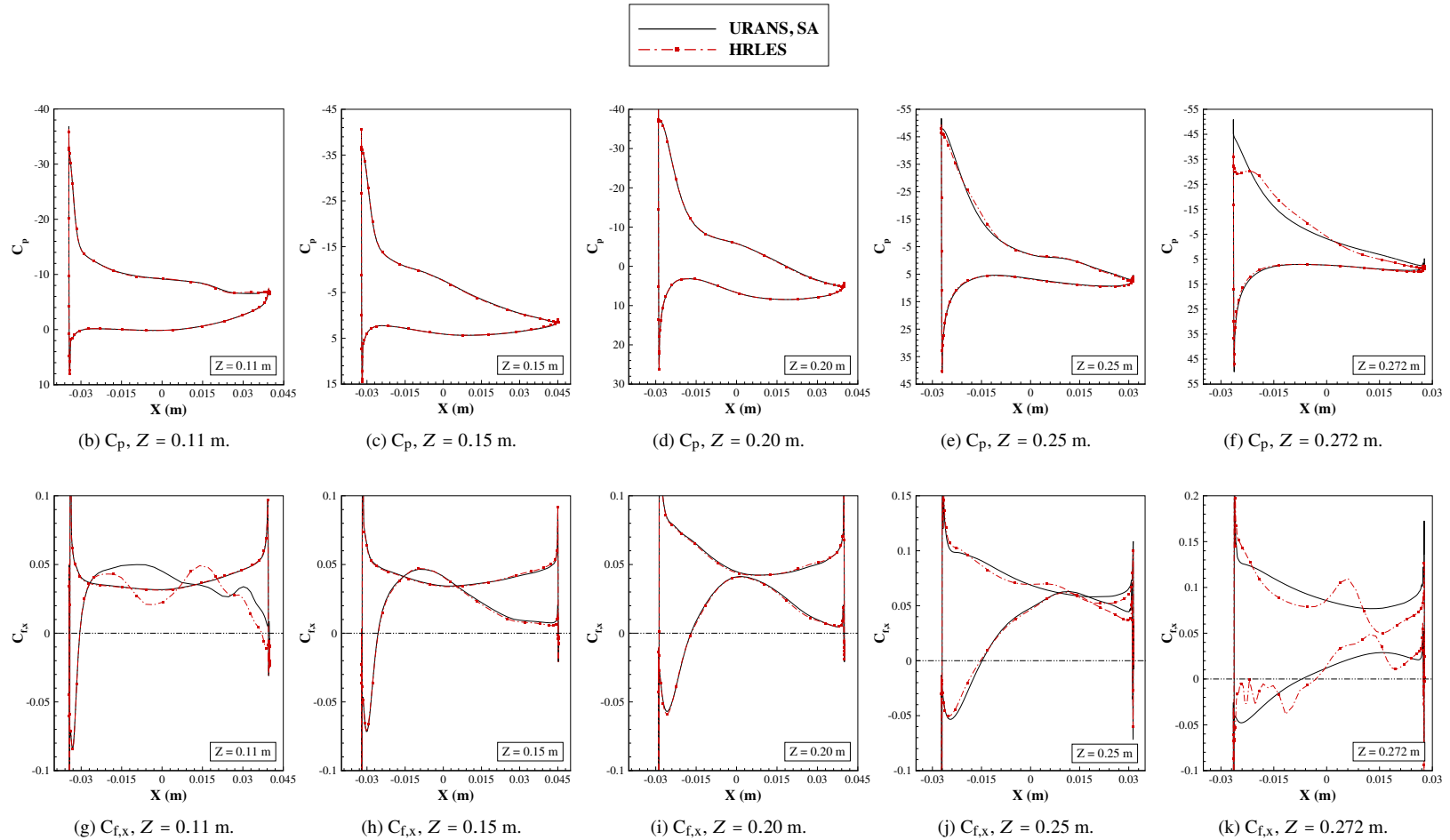
Fig. C.1 Comparison of pressure coefficient (C_p) and axial skin friction coefficient ($C_{f,x}$) surface profiles taken at different spanwise sections along the blade for the two flow models on the low-speed regime.

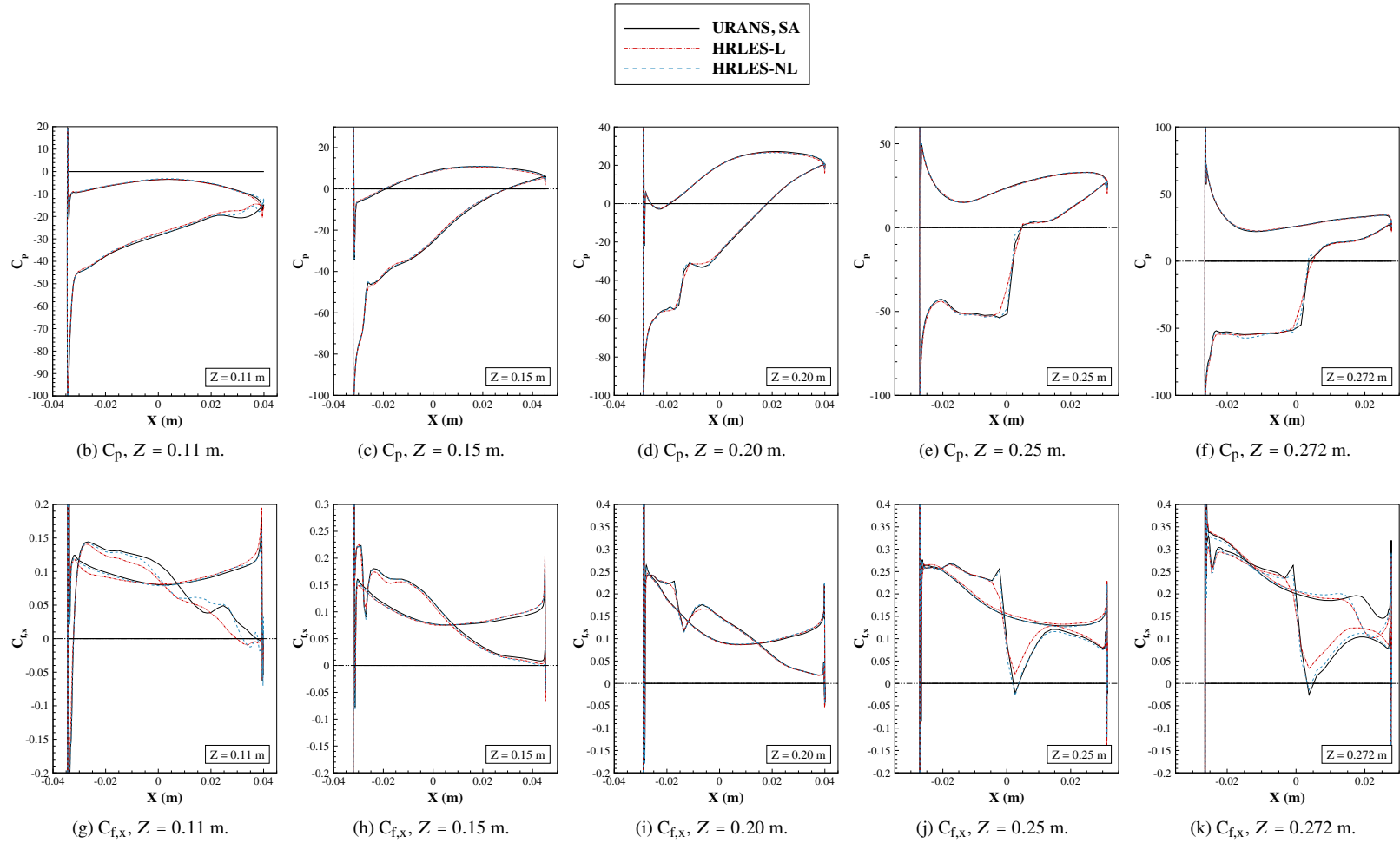# D. High-Speed Regime C_p and $C_{f,x}$ Blade Surface Profiles

Fig. D.1 Comparison of pressure coefficient (C_p) and axial skin friction coefficient ($C_{f,x}$) surface profiles taken at different spanwise sections along the blade for the two flow models on the high-speed regime.